Friction-damage coupled models and macroscopic strength criteria for ice-saturated frozen silt with crack asperity variation by a micromechanical approach

Lun-Yang Zhao, Yuan-Ming Lai, Jian-Fu Shao, Wan-Lu Zhang, Qi-Zhi Zhu, Fu-Jun Niu

▶ **To cite this version:**

Lun-Yang Zhao, Yuan-Ming Lai, Jian-Fu Shao, Wan-Lu Zhang, Qi-Zhi Zhu, et al.. Friction-damage coupled models and macroscopic strength criteria for ice-saturated frozen silt with crack asperity variation by a micromechanical approach. Engineering Geology, 2021, 294, ⟨10.1016/j.enggeo.2021.106405⟩. ⟨hal-04508817⟩

HAL Id: hal-04508817

https://hal.science/hal-04508817v1

Submitted on 22 Jul 2024

HAL is a multi-disciplinary open access archive for the deposit and dissemination of scientific research documents, whether they are published or not. The documents may come from teaching and research institutions in France or abroad, or from public or private research centers.

L'archive ouverte pluridisciplinaire **HAL**, est destinée au dépôt et à la diffusion de documents scientifiques de niveau recherche, publiés ou non, émanant des établissements d'enseignement et de recherche français ou étrangers, des laboratoires publics ou privés.

Distributed under a Creative Commons CC BY-NC 4.0 - Attribution - Non-commercial use - International License

Version of Record: https://www.sciencedirect.com/science/article/pii/S0013795221004166
Manuscript_83b15dc068c3622bbf61517a5a4079a7

Friction-damage coupled models and macroscopic strength criteria for ice-saturated frozen silt with crack asperity variation by a micromechanical approach

Lun-Yang Zhao[a,b], Yuan-Ming Lai[a,c,*], Jian-Fu Shao[b,*], Wan-Lu Zhang[d], Qi-Zhi Zhu[e], Fu-Jun Niu[a,c]

[a] *South China Research Institute on Geotechnical Engineering, School of Civil Engineering and Transportation, South China University of Technology, Guangzhou, 510641, China*
[b] *University of Lille, Centrale Lille, CNRS, UMR8107, LaMcube, 59000 Lille, France*
[c] *State Key Laboratory Frozen Soil Engineering, Cold and Arid Region Environmental and Engineering Institute, Chinese Academy of Sciences, Lanzhou, Gansu 730000, China*
[d] *Guangdong Key Laboratory of Integrated Agro-environmental Pollution Control and Management, Guangdong Engineering Center of Non-point Source Pollution Prevention Technology, Guangdong Institute of Eco-environment Science & Technology, Guangzhou, 510650, China*
[e] *Institute of Civil and Transportation Engineering, Hohai University, Nanjing, 210098 China*

Abstract

This paper aims to present physical friction-damage coupled models and derive macroscopic nonlinear strength criteria for ice-saturated frozen silt. Two material scales are considered here. The material at the mesoscale is composed of a frozen silt matrix and embedded mesocracks. At the microscale, the frozen silt matrix is composed of elastic mineral grains and elastic ice crystals. Considering this microstructure, for the ice-saturated frozen silt, the plastic deformation is related to frictional sliding along the mesocracks, and damage is due to the propagation of mesocracks. We obtain the effective elastic properties with a two-step linear Mori-Tanaka homogenization procedure. For the second homogenization step, we deduce the macroscopic stress-strain relations and local thermodynamic forces associated with damage and plasticity. Then, an energy release-based damage criterion is developed to capture the evolution of damage, and a friction sliding criterion with an associated/nonassociated local plastic flow rule is introduced to describe the rate of plasticity. The friction sliding criterion considers the variation of surface asperities of mesocracks as a result of pressure melting and damage evolution. In this context, associated/nonassociated multiscale friction-damage models are established. Furthermore, associated/nonassociated macroscopic nonlinear strength criteria as inherent parts of the corresponding multiscale models are derived under a large range of compressive stresses. For application, a semi-implicit local numerical algorithm of the multiscale models is developed. The accuracy of associated/nonassociated multiscale models is assessed by comparing their numerical simulations with conventional triaxial compression (CTC) tests. Although the associated multiscale model correctly predicts the nonlinear strength

© 2021 published by Elsevier. This manuscript is made available under the CC BY NC user license
https://creativecommons.org/licenses/by-nc/4.0/

behavior and axial deformation of the Lanzhou frozen silt under CTC tests with different temperatures, it fails to quantitatively reproduce volumetric deformation. Nonassociated multiscale model predictions with experimental data of volumetric deformation are significantly improved compared to the associated multiscale model.

Keywords: Frozen silt, Permafrost area, Friction-damage modeling, Strength criteria, Homogenization techniques

1. Introduction

The permafrost area in the world is 3.576×10^7 km^2, which constitutes 24% of the world's land surface(French, 2017). Frozen soil refers to the soil and rocks under temperatures below 0°C and contain some ice crystals (Lai et al., 2013, Zhang et al., 2001); they are typical heterogeneous materials including ice crystals, mineral grains, unfrozen water, and gases (Anderson and Morgenstern, 1973, Zhu et al., 2016b). Due to the highly rheological, temperature- and pressure-sensitive of ice crystals, frozen soil has more complex mechanical behaviors than unfrozen soil(Parameswaran, 1985, 1987, Zhu et al., 2016b, Lai et al., 2014). Recently, various types of infrastructure such as high-speed railways and roads are built in the cold region, which requires an in-depth study of the deformation and strength behavior of frozen soil. In addition, with the wide application of the artificial freezing method in subway engineering, tunnels, and other underground engineering activities(Russo et al., 2015, Tounsi et al., 2019), the stability of frozen soil engineering under high confining pressure plays a critical part in engineering construction. To this end, constitutive modeling and strength criteria under a wide range of compression stresses play an increasingly important role.

Experimental and theoretical investigations indicate that the macroscopic complex mechanical properties (e.g., nonlinear elastoplastic, anisotropic, rheological, and stress path influence) of frozen soil are directly reflected by its microscopic mechanical properties (Chang et al., 2008, Yang et al., 2010, Ma et al., 1999). Effective elastic properties of the frozen soil are connected with the elastic properties of each constituent phase and the volume fraction of each phase (Ning et al., 2005, Zhu et al., 2010b, Chang et al., 2019). In addition, the pores in the frozen soil and the weak interface between the phases are collectively referred to as cracks in the frozen soil(Lai et al., 2009, Zhu et al., 2016b, 2010b). Under the action of external loading and/or temperature, the variation of internal stress distribution in frozen soil will cause the initiation and propagation of cracks, which degrade the mechanical properties and eventually destroy the bearing capacity.

*Corresponding author
Email addresses: ymlai@lzb.ac.cn (Yuan-Ming Lai), jian-fu.shao@polytech-lille.fr (Jian-Fu Shao)

Therefore, the strength and nonlinear mechanical behaviors of frozen soil are closely related to the damage caused by the propagation of cracks (Ma et al., 1999, Zhao et al., 2017, Liu, 2005). In this context, one of the basic tasks of establishing the constitutive model and deriving the strength criterion of frozen soil is to accurately describe and simulate the heterogeneous system of ice crystals, mineral grains, unfrozen water and cracks.

Over the past few decades, researchers have developed various macroscopic models of the mechanical behaviors of frozen soil with nonlinear elasticity(Wang et al., 2004, Yang et al., 2010), plasticity(Lai et al., 2010, 2016), damage mechanics(Zhu et al., 2010b, Zhang et al., 2018c) and plastic-damage coupled theory(Lai et al., 2009), which are some representative studies. Several affecting factors on the mechanical properties of frozen soil have been considered in these models, such as the confining pressure, temperature, and strain rate. For example, Lai et al. (2009) developed a yield function that considered the hardening and softening effects of frozen sandy soil, and they proposed an elasto-plastic model based on generalized plasticity theory. Furthermore, Lai et al. (2016) established a new constitutive model of frozen saline sandy soil with rotational hardening multiple yield surface, which considered the initial and stress-induced anisotropy. In addition, Loria et al. (2017) proposed an elasto-plastic constitutive model with an elliptical and a parabolic yield surface and the associated flow rule to describe the nonlinear mechanical behavior of frozen soil. More recently, Zhao et al. (2020) proposed a bounding surface constitutive model for frozen saline soil, which considered the rotation of principal stress axes (RPSA). In these models, the frozen soil was usually regarded as a deformable solid, while the microstructure, local mechanical behavior and physical interactions of each phase were less emphasized, as discussed in Liu et al. (2018), Zhang et al. (2019b), Chang et al. (2019).

To date, most existing frozen soil strength criteria are basically obtained by fitting the results of laboratory tests. With the deepening of experimental research, the strength criterion has been developed from a linear criterion such as Drucker-Prager and Mohr-Comlomb to a nonlinear criterion. To describe the phenomenon where the frozen soil strength first increases and subsequently decreases with increasing confining pressure, various scholars have successively proposed the parabolic strength criteria(Ma et al., 1995, Fish, 1991), modified Mohr strength criteria(Yang et al., 2010, Qi and Ma, 2007), modified Hoek-Brown strength criteria(Zhang et al., 2018c), critical state strength criteria (Liao et al., 2016, Lai et al., 2016) and elliptic strength criteria(Zhang et al., 2017). Although these criteria can generally provide a good description of the frozen soil strength, few studied focus on deriving the nonlinear strength criterion of frozen soil from the micro- and (or) mesoscale to the macroscale.

Currently, considerable development has been made in establishing micromechanical-based models and deriving macroscopic strength criteria using different homogenization techniques for geomaterials at room temperature, such as soil, rock, and concrete (Zhao et al., 2018b,a, 2019,

Zhang et al., 2019b, Damiani and Sun, 2017, Dejaloud and Jafarian, 2017, Jin and Arson, 2018, Zhu et al., 2010a, Shen and Shao, 2018, Wu and Ju, 2017, Shen et al., 2018, Zhou and Meschke, 2018). These existing models and strength criteria consider the constitutive relationships and strength behaviors of constituent phases and take them to reproduce the existing test data of the heterogeneous materials. For example, Shen et al. (2018) established an approximate analytical macroscopic strength criterion of porous materials with a pressure-sensitive and tension-compression asymmetry solid matrix using the stress variational homogenization method (SVH). Wu and Ju (2017) developed an elasto-plastic damage micromechanical framework, which considered the fiber breakage to describe the macroscopic behaviors of continuous fiber-reinforced composites. Zhou and Meschke (2018) proposed a multiscale homogenization framework to predict the strength of fully and partially frozen soil using the linear comparison composite approach. Recently, Zhao et al. (2018b) established a micromechanical friction damage model for quasi-brittle material in the framework of thermodynamic and with Mori-Tanaka homogenization method. Afterward, a micromechanical friction-damage model(Zhao et al., 2018a) was developed to analyze the localized cracking in quasi-brittle materials. Generally, most of these constitutive models and strength criteria are suitable for reproducing the behaviors of unfrozen composites; however, few works account for the interactions with the multiple phases and the plastic and/or damage evolution caused by the growth of cracks in frozen soil.

In this work, physical associated and nonassociated multiscale friction-damage coupled models are developed, and corresponding strength criteria as an inherent part of the multiscale models are derived for the ice-saturated frozen silt. In contrast to existing models, the frozen silt in mesoscale is considered to be several families of mesocracks embedded in a frozen soil matrix, which is composed of elastic mineral grains and elastic ice crystals in microscale. For the investigated ice-saturated frozen silt, the particle size breakdown will not be taken into account, and the unfrozen water content will be neglected. For clarity, the outline of this paper is as follows: after a brief description of the ice-saturated frozen silt microstructure, the representative volume element (RVE) in each scale is chosen, and we estimate the effective elastic behavior using a two-step linear homogenization procedure (Section 2). In Section 3, using the thermodynamic framework and Mori-Tanaka homogenization scheme, the plastic and damage evolution is described by the associated/nonassociated multiscale friction-damage coupled models. Friction sliding criteria with associated/nonassociated local plastic flow rules are adopted. These models enable one to consider the effect of damage evolution and pressure melting on the change in surface asperity of mesocracks. Then, in Section 4, associated/nonassociated macroscopic strength criteria are derived. Finally, the numerical implementation of the associated/nonassociated multiscale models is developed, and the associated/nonassociated multiscale models and associated/nonassociated macroscopic strength criteria are validated on Lanzhou frozen silt in Section 5.

2. Microstructure and effective elastic properties of ice-saturated frozen silt

2.1. Description of the representative volume element (RVE)

The microstructure of ice-saturated frozen silt has been largely investigated in literature (Ma et al., 1999, Yershov, 2004). A scale separation is proposed based on the microtests with the scanning electronic microscope. Generally, three relevant scales are considered

- The macroscale ($\geq 10^{-1}$m), where frozen silt can be considered a homogeneous continuum (Yershov, 2004).
- The mesoscale ($10^{-4} \sim 10^{-1}$m), where mesocracks are embedded in the frozen silt matrix(Ma et al., 1999).
- The microscale ($\leq 10^{-4}$m), where the frozen silt matrix is composed of mineral grains and ice crystals, which are arbitrarily distributed inside the mineral grains (Yershov, 2004).

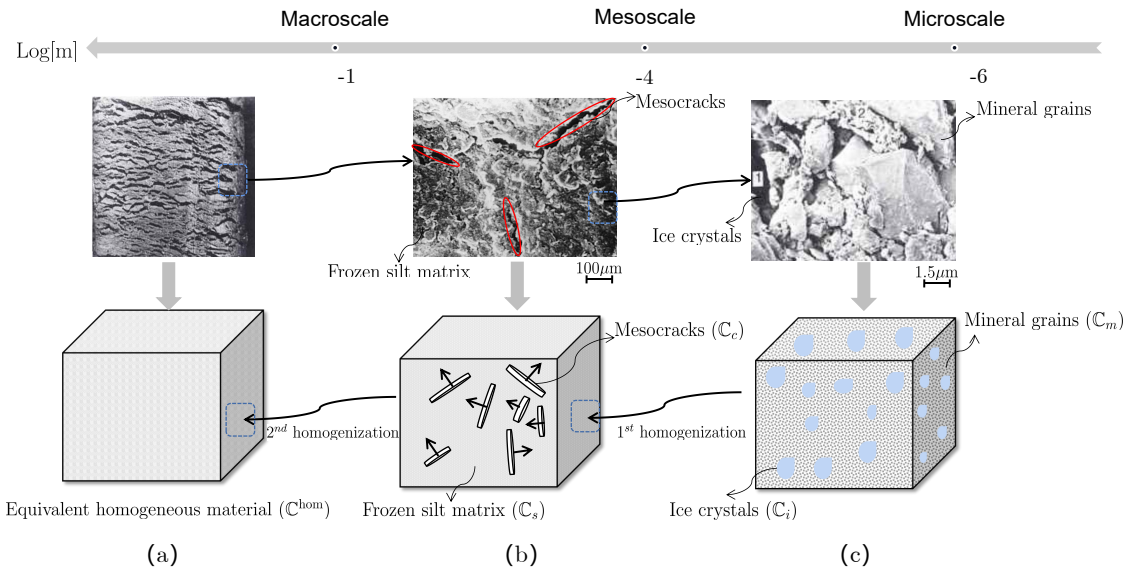

Figure 1: Microstructure and representative volume element of ice-saturated frozen silt in each scale

With this microstructure and scale separation, the representative volume element (RVE) in each scale can be defined, as shown in Figure 1. For clarity, the total volume of studied RVE (Figure 1b) is denoted by Ω, the volume of mesocracks is Ω_c, the volume of the frozen silt matrix is $\Omega_m + \Omega_i$, Ω_m is the volume of mineral grains, and Ω_i is the volume of ice crystals. In this case, the volume fraction of mesocracks ϕ_c at mesoscale and volume fraction of ice crystals φ_i at microscale can be defined as follows:

$$\phi_c = \frac{\Omega_c}{\Omega}, \quad \varphi_i = \frac{\Omega_i}{\Omega_i + \Omega_m} \tag{1}$$

The distribution of mesocracks is generally not isotropic but in certain privileged directions, which implies that an anisotropic description is necessary. The present theoretical framework can be used to describe such anisotropic cracking process by considering a spatial crack density distribution. However, for the sake of computational simplicity, an isotropic distribution of mesocracks is considered in this work. In the viewpoint of isotropic assumption, we define each penny-shaped mesocrack characterized by its aspect ratio ϵ ($\epsilon = c/a$, where a is the average radius, and c is the half opening) and unit normal vector $\underline{n}$. Then, the volume fraction ϕ_c^r of the r^{th} family of mesocracks is defined as $\phi_c^r = \frac{4}{3}\pi a^2 c\mathcal{N} = \frac{4}{3}\pi\epsilon d$, where $\mathcal{N}$ is the mesocrack density, referring to the number of mesocracks per unit volume, and $d = \mathcal{N}a^3$ is the damage density variable (Budiansky and O'connell, 1976). In this case, one has $\phi_c = \sum_r \phi_c^r$. Furthermore, to obtain an analytical solution of Eshelby's tensor for a penny-shaped mesocrack in an isotropic elastic solid matrix, we assume the mesocrack with a vanished aspect ratio.

2.2. *Estimation of effective elastic properties with two-step Mori-Tanaka homogenization scheme*

With the above assumption, the effective elastic properties of frozen silt are estimated using the homogenization scheme. Assume that the ice crystals and mineral grains obey a linear isotropic elastic behavior with elastic stiffness tensor $\mathbb{C}_i = 2\mu_i\mathbb{K} + 3k_i\mathbb{J}$ and $\mathbb{C}_m = 2\mu_m\mathbb{K} + 3k_m\mathbb{J}$, respectively. Here, $k_{i(m)} = \frac{E_{i(m)}}{3(1-2\nu_{i(m)})}$ and $\mu_{i(m)} = \frac{E_{i(m)}}{2(1+\nu_{i(m)})}$ represent the elastic bulk modulus and elastic shear modulus of ice crystals (subscript i) and mineral grains (subscript m) respectively; $E_{i(m)}$ and $\nu_{i(m)}$ are the elastic modulus and Poisson's ratio of ice crystals (subscript i) and mineral grains (subscript m).

A matrix-inclusion system is considered in the microscale (see Figure 1(c)). Here, we assume that ice crystals have a smaller volume fraction than mineral grains, which implies that mineral grains are considered the matrix, and ice crystals are the inclusions. In this context, Mori-Tanaka homogenization approach (Mori and Tanaka, 1973) can be directly employed in the 1^{st} homogenization step to obtain the frozen silt matrix elastic stiffness tensor

$$\mathbb{C}_s = 3k_s\mathbb{J} + 2\mu_s\mathbb{K} \tag{2}$$

where the effective elastic bulk modulus k_s and elastic shear modulus μ_s are expressed as follows

$$k_s = \frac{3k_mk_i + 4(1-\varphi_i)k_m\mu_m + 4\varphi_ik_i\mu_m}{3\varphi_ik_m + 3(1-\varphi_i)k_i + 4\mu_m} \tag{3a}$$

$$\mu_s = \frac{\mu_m\left(k_m\left(\mu_i\left(9\varphi_i+6\right) - 9\left(\varphi_i-1\right)\mu_m\right) + 4\mu_m\left(\mu_i\left(2\varphi_i+3\right) - 2\left(\varphi_i-1\right)\mu_m\right)\right)}{-6\varphi_i\left(\mu_i-\mu_m\right)\left(k_m+2\mu_m\right) + 6\mu_ik_m + 12\mu_i\mu_m + 9k_m\mu_m + 8\mu_m^2} \tag{3b}$$

Figure 2 illustrates the evolution of k_s and μ_s of the frozen silt matrix with an increasing volume fraction of ice crystals φ_i. Here, we take $E_m = 100$ MPa, $\nu_m = 0.25$, and $E_i = 6500$ MPa $\nu_m = 0.3$. With the increase in volume fraction of ice crystals, both k_s and μ_s tend to increase.

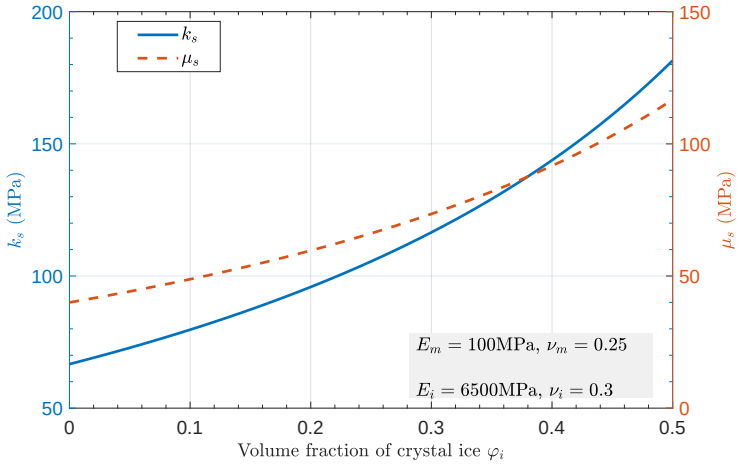

Figure 2: Effect of the volume fraction of crystal ice on the elastic behavior of the frozen silt matrix

For the 2^{nd} homogenization step, the RVE is a matrix-crack system (see Figure 1(b)). The elastic tensor $\mathbb{C}_s$ of frozen silt matrix has been obtained in the 1^{st} homogenization step. The stiffness tensor $\mathbb{C}_c^r$ depends on the state of the r^{th} family of mesocracks, which will be introduced later. For this RVE, the general effective elastic tensor is derived (Zaoui, 1997, Zhu et al., 2011)

$$\mathbb{C}_{\text{hom}} = \mathbb{C}_s + \sum_r \phi_c^r (\mathbb{C}_c^r - \mathbb{C}_s) : \mathbb{A}_c^r = \mathbb{C}_s + \bar{\mathbb{A}}_c : (\mathbb{C}_c - \mathbb{C}_s) \tag{4}$$

The second equation in Eq. (4) results from the isotropic distribution of mesocracks, where $\bar{\mathbb{A}}_c = \sum_r \phi_c^r \mathbb{A}_c^r$, and one assumes $\mathbb{C}_c^r = \mathbb{C}_c$. In Eq. (4), $\mathbb{A}_c^r$ is the average strain concentration tensor of r^{th} family mesocracks. The determination of $\mathbb{A}_c^r$ relies on the homogenization method. Here, Mori-Tanaka homogenization method is employed again

$$\mathbb{A}_c^r = [\mathbb{I} + \mathbb{H} : (\mathbb{C}_c^r - \mathbb{C}_m)]^{-1} : \left[(1-\phi_c)\mathbb{I} + \sum_{r=1} \phi_c^r [\mathbb{I} + \mathbb{H} : (\mathbb{C}_c^r - \mathbb{C}_m)]^{-1}\right]^{-1} \tag{5}$$

where the fourth-order Hill's tensor $\mathbb{H}$ can be directly related to Eshelby tensor with $\mathbb{E} = \mathbb{H} : \mathbb{C}_s$. For open penny-shaped mesocracks, $\mathbb{C}_c$ vanishes, the strain concentration tensor $\bar{\mathbb{A}}_c$ is expressed as

$$\bar{\mathbb{A}}_c = \frac{Q_1 d}{1 + Q_1 d}\mathbb{J} + \frac{Q_2 d}{1 + Q_2 d}\mathbb{K} \tag{6}$$

where $Q_1 = \frac{16}{9}\frac{1-\nu_s^2}{1-2\nu_s}$ and $Q_2 = \frac{32}{45}\frac{(1-\nu_s)(5-\nu_s)}{2-\nu_s}$ are connected with the Poisson's ratio of the frozen silt matrix ν_s (Zhao et al., 2018b, Zhu et al., 2011). By substituting Eq. (6) into Eq. (4), one can obtain the effective stiffness tensor $\mathbb{C}_{\text{hom}}$ for ice-saturated frozen silt with opened mesocracks

$$\mathbb{C}_{\text{hom}} = 3k_{\text{hom}}\mathbb{J} + 2\mu_{\text{hom}}\mathbb{K} \tag{7}$$

where k_{hom} and μ_{hom} are the effective bulk modulus and shear modulus, respectively, which read

$$k_{\text{hom}} = k_s\left(1 - \frac{Q_1 d}{1 + Q_1 d}\right), \quad \mu_{\text{hom}} = \mu_s\left(1 - \frac{Q_2 d}{1 + Q_2 d}\right) \tag{8}$$

Then, the effective elastic compliance tensor $\mathbb{M}_{\text{hom}}$ is

$$\mathbb{M}_{\text{hom}} = (\mathbb{C}_{\text{hom}})^{-1} = \mathbb{M}_s + \mathbb{M}_d, \quad \text{with } \mathbb{M}_d = \frac{Q_1 d}{3k_s}\mathbb{J} + \frac{Q_2 d}{2\mu_s}\mathbb{K} \tag{9}$$

where $\mathbb{M}_s$ is the elastic compliance of the frozen silt matrix, and $\mathbb{M}_d$ is the additional compliance induced by mesocracks.

Figure 3 illustrates the effective bulk modulus k_{hom} and shear modulus μ_{hom} with damage evolution. One can see that with the increase of damage, both k_{hom} and μ_{hom} rapidly decrease.

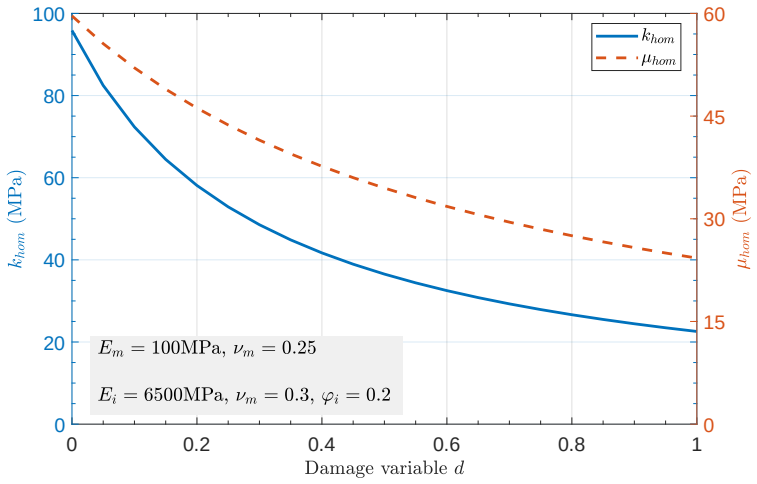

Figure 3: Illustration of the evolution of the effective bulk modulus and shear modulus with damage

3. Plastic and damage description with associated/nonassociated multiscale friction-damage models

The damage evolution and plastic deformation of ice-saturated frozen silt under compressive stresses are described in this section using the associated and nonassociated multiscale friction-damage models, respectively. We assume all closed and elastically cemented mesocracks in this case, and no elastic displacement discontinuities occur along the crack surfaces. Furthermore, each mesocrack is a rough surface described by a local frictional coefficient. The asperity of the mesocrack surface varies with the crack slip and pressure melting of ice crystals. Frictional sliding occurs only when local stresses applied on the crack surfaces yield a specific friction criterion,

which produces plastic strains at the macroscale. Without loss of generality, both frictional criteria with associated and nonassociated local plastic flow rules are introduced. In addition, the damage criterion relevant to the propagation of mesocracks is proposed to describe the damage evolution. With the hypothesis of small strains and isothermal conditions, the total strain tensor can be separated into two parts:

$$\boldsymbol{E} = \boldsymbol{E}^e + \boldsymbol{E}^p. \tag{10}$$

where elastic strain $\boldsymbol{E}^e$ is the deformation of the frozen silt matrix, and $\boldsymbol{E}^p$ belongs to the frictional sliding along closed mesocracks.

3.1. Thermodynamics framework

Using the strain decomposition and the results of previous works (Zhu et al., 2011, Zhao et al., 2018b), the free energy of cracked frozen silt is

$$\Pi = \underbrace{\frac{1}{2}(\boldsymbol{E} - \boldsymbol{E}^p) : \mathbb{C}_s : (\boldsymbol{E} - \boldsymbol{E}^p)}_{\Pi^e} + \underbrace{\frac{1}{2}\boldsymbol{E}^p : \mathbb{C}_d : \boldsymbol{E}^p}_{\Pi^p}. \tag{11}$$

where Π^e is the elastic free energy of the frozen silt matrix, and Π^p is the stored energy related to the frictional sliding along closed mesocracks. $\mathbb{C}_d$ is a fourth-order tensor considering the coupling between the propagation and the frictional sliding of mesocracks. The expression of $\mathbb{C}_d$ has been derived in previous works (Zhu, 2016, Zhao et al., 2018b)

$$\mathbb{C}_d = (\mathbb{M}_d)^{-1} = \frac{3k_s}{Q_1 d}\mathbb{J} + \frac{2\mu_s}{Q_2 d}\mathbb{K} \tag{12}$$

Considering the second law of thermodynamic, Clausius-Duhem inequality is

$$\boldsymbol{\Sigma} : \dot{\boldsymbol{E}} - \dot{\Pi} = \left(\boldsymbol{\Sigma} - \frac{\partial \Pi}{\partial \boldsymbol{E}}\right) : \dot{\boldsymbol{E}} - \frac{\partial \Pi}{\partial \boldsymbol{E}^p} : \dot{\boldsymbol{E}}^p - \frac{\partial \Pi}{\partial d}\dot{d} \geq 0 \tag{13}$$

Thus, the macroscopic stress-strain relationship can be derived as follows:

$$\boldsymbol{\Sigma} = \frac{\partial \Pi}{\partial \boldsymbol{E}} = \mathbb{C}_s : (\boldsymbol{E} - \boldsymbol{E}^p), \tag{14}$$

and the thermodynamic forces associated with $\boldsymbol{E}^p$ and d can be obtained:

$$\boldsymbol{\Sigma}^c = -\frac{\partial \Pi}{\partial \boldsymbol{E}^p} = \boldsymbol{\Sigma} - \mathbb{C}_d : \boldsymbol{E}^p \tag{15}$$

$$\mathcal{Y}_d = -\frac{\partial \Pi}{\partial d} = \frac{1}{2}\boldsymbol{E}^p : \frac{\partial \mathbb{C}_d}{\partial d} : \boldsymbol{E}^p, \tag{16}$$

Local stress $\boldsymbol{\Sigma}^c$ applied onto mesocracks is the driving force of frictional sliding. Eq. (15) shows that $\boldsymbol{\Sigma}^c$ relates to the damage variable d, which implies that the damage evolution inherently affects

the plastic deformation contribute to frictional sliding.The local stress $\boldsymbol{\Sigma}^c$ accounts for mesocracks interactions by introducing the fourth-order tensor $\mathbb{C}_d$. Furthermore, Eq. (16) shows that the damage conjugated thermodynamic force $\mathcal{Y}_d$ directly relates to the plastic strain tensor $\boldsymbol{E}^p$. Consequently, the damage growth is directly controlled by plastic deformations. All mesocracks are assumed to be elastically glued due to the roughness of asperities on crack surfaces. The plastic frictional sliding is the unique cause of displacement discontinuity along the mesocracks and the driving force of crack propagation.

3.2. Damage criterion

To capture the damage evolution related to the propagation of mesocracks, the local damage criterion proposed in (Zhao et al., 2018b) is employed here:

$$\mathcal{D}(\mathcal{Y}_d, d) = \mathcal{Y}_d - \mathcal{R}(d) \leq 0, \tag{17}$$

where $\mathcal{R}(d)$ is the current resistance to damage evolution (mesocrack propagation) of the frozen silt. According to the previous work (Zhao et al., 2018b), the specific form is followed

$$\mathcal{R}(d) = \mathcal{R}_c g(\varsigma) \ , \ \varsigma = \frac{d}{d_c}, g(\varsigma) = \frac{2\varsigma}{1+\varsigma^2} \tag{18}$$

where d_c is the critical value of damage density variable when the peak strength reaches. $\mathcal{R}_c$ is the maximal value of $\mathcal{R}(d)$ when $d = d_c$. Thus, the material toughness to mesocrack propagation reaches its maximal value $\mathcal{R}_c$ when the damage d reaches the critical value d_c.

With the damage criterion at hand, the evolution of damage can be determined with the following normality rule:

$$\dot{d} = \lambda^d \frac{\partial \mathcal{D}}{\partial \mathcal{Y}_d} = \lambda^d, \tag{19}$$

where λ^d is the nonnegative damage multiplier. It will be determined by the damage consistency condition in Section 5.1.1.

3.3. Friction criterion with an associated local plastic flow rule

Analogous to the macroscopic plastic theory, the plastic deformation associated with local frictional sliding can be controlled by a yield criterion and plastic flow rule. Because the frictional sliding is controlled by the local stress tensor $\boldsymbol{\Sigma}^c$, the classical Coulomb-type friction criterion at the local mesoscale is adopted, i.e.,

$$\mathcal{F}(\boldsymbol{\Sigma}^c) = \|\boldsymbol{S}^c\| + \eta P^c \leq 0, \tag{20}$$

where $P^c = \frac{1}{3}\boldsymbol{\Sigma}^c : \boldsymbol{\delta}$ and $\boldsymbol{S}^c = \mathbb{K} : \boldsymbol{\Sigma}^c$ are the local mean stress and deviatoric stress, respectively. Parameter η is the local friction coefficient of mesocracks surfaces, which is related to the

physical roughness of crack surfaces. Before localization, a higher degree of interlocking of asperities occurs with the progress of frictional sliding of mesocracks. However, after localization, with the frictional sliding of localized crack, asperities of crack surfaces are gradually destroyed (Krabbenhoft et al., 2012, Zhao et al., 2018a). Consequently, the friction coefficient η reasonably increase at the pre-peak regime and subsequently decrease at post-peak regime, which implies that the local friction coefficient increases when $d \leq d_c$ and decreases when $d > d_c$. In addition, with the increase in mean stress Σ_m, the pressure melting of ice crystals and water migration provide a lubrication process on the crack surfaces, which reduces the surface roughness(Ma et al., 1999, Nielsen et al., 2010). Based on the above analysis and considering the previous results in (Zhao et al., 2018b), we propose the following relation to capturing the change in local friction coefficient η with mean stress Σ_m and damage d. To avoid introducing additional parameters, the function $g(\varsigma)$ is adopted here

$$\eta = \alpha\eta_m + (1-\alpha)\,\eta_m g(\varsigma), \quad \text{with} \quad \eta_m = \eta_c \exp(b\frac{\Sigma_m}{P_a}) \tag{21}$$

where η_c is the friction coefficient without considering the pressure melting effect and damage evolution, η_m is the friction coefficient that only captures the pressure melting effect, parameter α relates to the initial value of friction coefficient, parameter b controls the friction coefficient degradation rate with increasing mean stress Σ_m, and $P_a = 0.10133$ MPa is the standard atmospheric pressure. Obviously, when d reaches d_c, $\eta = \eta_m$. For the convenience of understanding, Figure 4 depicts the variation of friction coefficient η with damage variable d and mean Σ_m.

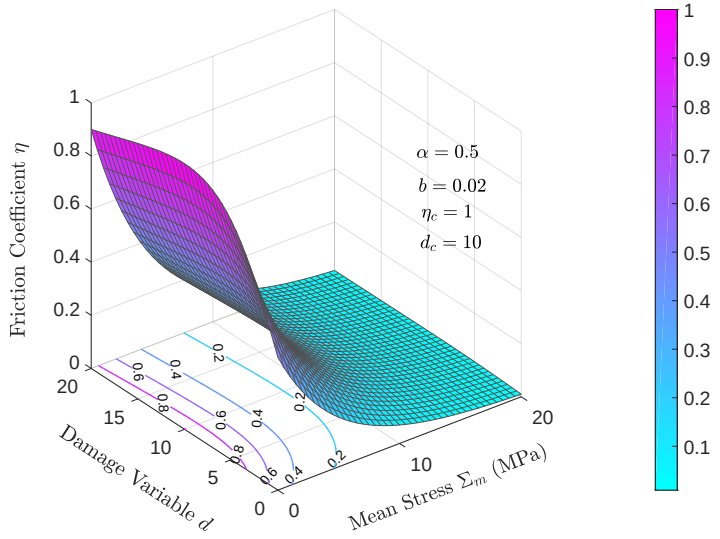

Figure 4: Evolution of friction coefficient η with the change in damage variable d and mean macroscopic stress Σ_m

Then, we adopt an associated local plastic flow rule in the thermodynamic framework to de-

velop an associated multiscale friction-damage coupled model. The rate of plastic strain associated with frictional sliding can be obtained by using the normality rule:

$$\dot{\boldsymbol{E}}^p = \lambda^p \frac{\partial \mathcal{F}}{\partial \boldsymbol{\Sigma}^c} = \lambda^p \boldsymbol{N}_a, \tag{22}$$

where λ^p is the plastic multiplier, which will be determined from the consistency conditions discussed in Section 5.1. $\boldsymbol{N}_a$ is the plastic flow direction with the following expression:

$$\boldsymbol{N}_a = \frac{\boldsymbol{S}^c}{\|\boldsymbol{S}^c\|} + \frac{\eta}{3}\left(1 + \frac{b}{P_a}\right)\boldsymbol{\delta} = \boldsymbol{T} + \frac{\eta}{3}\left(1 + \frac{b}{P_a}\right)\boldsymbol{\delta}. \tag{23}$$

3.4. Friction criterion with a nonassociated local plastic flow rule

Without loss of generality, we also consider a nonassociated local plastic flow rule to capture the flow direction of plastic strain and develop a nonassociated multiscale friction-damage coupled model. Here, we introduce a nonassociated plastic potential, i.e.,

$$\mathcal{G}(\boldsymbol{\Sigma}^c) = \|\boldsymbol{S}^c\| + \kappa P^c \le 0, \tag{24}$$

where κ is the dilation parameter. To ensure the nonassociated macroscopic strength criterion in the following work, κ should remain constant. In this case, the rate of plastic strain yields

$$\dot{\boldsymbol{E}}^p = \lambda^p \frac{\partial \mathcal{G}}{\partial \boldsymbol{\Sigma}^c} = \lambda^p \boldsymbol{N}_n, \tag{25}$$

where $\boldsymbol{N}_n = \boldsymbol{T} + \frac{\kappa}{3}$ is the local plastic flow direction.

4. Associated/nonassociated macroscopic strength criteria

In this section, to capture the strength behavior of frozen silt, we shall derive associated/nonassociated macroscopic strength criteria as an inherent part of the corresponding associated/nonassociated multiscale friction-damage models.

4.1. Derivation of an associated macroscopic strength criterion

For the monotonic loading paths (e.g., conventional triaxial compression, lateral extension, and proportional compression), the principal stress directions will not rotate. In these cases, the shear flow direction $\boldsymbol{T}$ in Eq. (23) is unchanged (Zhu, 2016), and the plastic strain $\boldsymbol{E}^p$ can be reformulated as

$$\boldsymbol{E}^p = \int \dot{\boldsymbol{E}}^p = \int \lambda^p \boldsymbol{N}_a = \Lambda^p \boldsymbol{T} + \frac{1}{3}\Xi\boldsymbol{\delta} \tag{26}$$

where $\Lambda^p = \int \lambda^p$ is the accumulated plastic multiplier, and $\Xi = \int \lambda^p \eta\left(1 + \frac{b}{P_a}\right) = \mathrm{tr}\boldsymbol{E}^p$. Accordingly, the thermodynamic forces (15) and (16) can be rewritten as

$$\boldsymbol{\Sigma}^c = \boldsymbol{\Sigma} - \varkappa_1 \frac{\Xi}{d}\boldsymbol{\delta} - \varkappa_2 \frac{\Lambda^p}{d}\boldsymbol{T}, \text{ with } \varkappa_1 = \frac{k_s}{Q_1}, \varkappa_2 = \frac{2\mu_s}{Q_2} \tag{27}$$

$$\mathcal{Y}_d = \frac{1}{2}\left[\varkappa_1\left(\frac{\Xi}{d}\right)^2 + \varkappa_2\left(\frac{\Lambda^p}{d}\right)^2\right] \tag{28}$$

Then, the friction criterion (20) and damage criterion (17) can be reformulated as

$$\mathcal{F}\left(\boldsymbol{\Sigma}^c\right) = \mathcal{F}\left(\boldsymbol{\Sigma}, \Xi, \Lambda^p, d\right) = \|\boldsymbol{S}\| + \eta\Sigma_m - \left(\varkappa_1\eta\frac{\Xi}{d} + \varkappa_2\frac{\Lambda^p}{d}\right) \leq 0 \tag{29}$$

$$\mathcal{D}(\mathcal{Y}_d, d) = \mathcal{D}(\Xi, \Lambda^p, d) = \frac{1}{2}\left[\varkappa_1\left(\frac{\Xi}{d}\right)^2 + \varkappa_2\left(\frac{\Lambda^p}{d}\right)^2\right] - \mathcal{R}(d) \leq 0 \tag{30}$$

As noted in Section 3.2, when damage reaches its critical value d_c, $\mathcal{R}(d)$ takes its maximal value $\mathcal{R}_c$, and the failure of frozen silt occurs. In this context, the plastic deformation at peak stress state yields

$$\begin{aligned} & \max_{\Xi,\Lambda^p}\left(\varkappa_1\eta_m\frac{\Xi}{d_c} + \varkappa_2\frac{\Lambda^p}{d_c}\right) \\ \text{subject to } \mathcal{D}(\Xi, \Lambda^p) \quad = \quad & \frac{1}{2}\left[\varkappa_1\left(\frac{\Xi}{d_c}\right)^2 + \varkappa_2\left(\frac{\Lambda^p}{d_c}\right)^2\right] - \mathcal{R}_c = 0 \end{aligned} \tag{31}$$

The Lagrangian associated with (31) is given by

$$\mathcal{L}\left(\Xi, \Lambda^p, \lambda\right) = \varkappa_1\eta_m\frac{\Xi}{d_c} + \varkappa_2\frac{\Lambda^p}{d_c} - \lambda\left[\varkappa_1\left(\frac{\Xi}{d_c}\right)^2 + \varkappa_2\left(\frac{\Lambda^p}{d_c}\right)^2 - 2\mathcal{R}_c\right] \tag{32}$$

where λ is a Lagrange multiplier.

Then, one has the following first-order Karush-Kuhn-Tucker optimality conditions:

$$\nabla_\Xi\mathcal{L} = \varkappa_1\eta_m - 2\lambda\varkappa_1\frac{\Xi}{d_c} = 0 \tag{33a}$$

$$\nabla_{\Lambda^p}\mathcal{L} = \varkappa_2 - 2\lambda\varkappa_2\frac{\Lambda^p}{d} = 0 \tag{33b}$$

$$\nabla_\lambda\mathcal{L} = -\varkappa_1\left(\frac{\Xi}{d_c}\right)^2 - \varkappa_2\left(\frac{\Lambda^p}{d_c}\right)^2 + 2\mathcal{R}_c = 0 \tag{33c}$$

By solving Eq. (33), one obtains

$$\frac{\Xi}{d_c} = \eta_m\sqrt{\frac{2\mathcal{R}_c}{\varkappa_1\eta_m^2 + \varkappa_2}}, \quad \frac{\Lambda^p}{d_c} = \sqrt{\frac{2\mathcal{R}_c}{\varkappa_1\eta_m^2 + \varkappa_2}} \tag{34}$$

Then, the maximum value of

$$\max_{\Xi,\Lambda^p}\left(\varkappa_1\eta_m\frac{\Xi}{d_c} + \varkappa_2\frac{\Lambda^p}{d_c}\right) = \sqrt{2\mathcal{R}_c\left(\varkappa_1\eta_m^2 + \varkappa_2\right)} \tag{35}$$

By inserting Eq. (35) into (29), we can convert the failure criterion of frozen silt into the following form

$$\mathcal{F}(\boldsymbol{\Sigma}) = \|\boldsymbol{S}\| + \eta_m \Sigma_m - \sqrt{2\mathcal{R}_c\left(\varkappa_1 \eta_m^2 + \varkappa_2\right)} = 0 \tag{36}$$

Under the sign convention of geomechanics, the associated macroscopic strength criterion in the meridian plane ($\Sigma_m - \Sigma_d$ plane) is derived as follows

$$\Sigma_d = \sqrt{\frac{3}{2}}\eta_c \exp\left(-b\frac{\Sigma_m}{P_a}\right)\Sigma_m + \sqrt{3\mathcal{R}_c\left[\varkappa_1 \eta_c^2 \exp\left(-2b\frac{\Sigma_m}{P_a}\right) + \varkappa_2\right]} \tag{37}$$

where $\Sigma_d = \sqrt{\frac{3}{2}}\|\boldsymbol{S}\|$ is the macroscopic deviatoric stress.

A graphical representation of the derived nonlinear strength criterion (Eq. (37)) is given in Figure 5. The derived associated strength criterion exhibits apparent nonlinearity in the ($\Sigma_m - \Sigma_d$) plane. With the increase in mean stress Σ_m, the strength first increases and subsequently decreases. This result is consistent with the previous works of Liao et al. (2016), Liu et al. (2019a,b), Ma et al. (1999), Qi and Ma (2007)

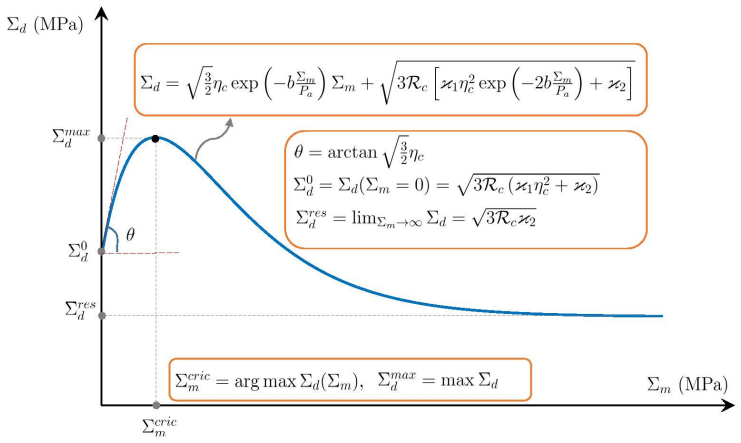

Figure 5: Graphical representation of the derived associated macroscopic strength criterion (37) in the merdian plane ($\Sigma_m - \Sigma_d$ plane)

4.2. Derivation of a nonassociated macroscopic strength criterion

If the principal stress directions are fixed, the plastic flow direction $\boldsymbol{N}_n$ for the nonassociated local plastic flow rule does not change. Accordingly, one obtains the accumulated plastic strain

$$\boldsymbol{E}^p = \int \dot{\boldsymbol{E}}^p = \int \lambda^p \boldsymbol{N}_n = \Lambda^p\left(\boldsymbol{T} + \frac{1}{3}\kappa\boldsymbol{\delta}\right) \tag{38}$$

Then, the friction criterion (20) and damage criterion (17) can be rewritten as follows

$$\mathcal{F}(\boldsymbol{\Sigma}^c) = \mathcal{F}(\boldsymbol{\Sigma}, \Lambda^p, d) = \|\boldsymbol{S}\| + \eta\Sigma_m - \left(\varkappa_1\eta\frac{\kappa\Lambda^p}{d} + \varkappa_2\frac{\Lambda^p}{d}\right) \le 0 \tag{39}$$

$$\mathcal{D}(\mathcal{Y}_d, d) = \mathcal{D}(\Xi, \Lambda^p, d) = \frac{1}{2}\left[\varkappa_1\left(\frac{\kappa\Lambda^p}{d}\right)^2 + \varkappa_2\left(\frac{\Lambda^p}{d}\right)^2\right] - \mathcal{R}(d) \leq 0, \tag{40}$$

By solving Eq. (40) when the equal sign is true, one obtains

$$\frac{\Lambda^p}{d} = \sqrt{\frac{2\mathcal{R}(d)}{\varkappa_1\kappa^2 + \varkappa_2}} \tag{41}$$

Substituting Eq. (41) into (39) and considering peak compression strength reached when $d = d_c$, one can obtain a nonassociated macroscopic strength criterion in $(\Sigma_m - \Sigma_d)$ plane

$$\Sigma_d = \sqrt{\frac{3}{2}}\eta_c \exp\left(-b\frac{\Sigma_m}{P_a}\right)\Sigma_m + \left[\varkappa_1\eta_c \exp\left(-b\frac{\Sigma_m}{P_a}\right)\kappa + \varkappa_2\right]\sqrt{\frac{3\mathcal{R}_c}{\varkappa_1\kappa^2 + \varkappa_2}} \tag{42}$$

Comparing the associated strength criterion (37) and the nonassociated strength criterion (42), one can see that the nonassociated strength criterion is additionally related to the dilation parameter κ.

5. Numerical implementation and model validation

To evaluate the performances of the proposed associated/nonassociated multiscale models and the derived associated/nonassociated strength criteria, we first give the numerical implementations of the models; then, the mechanical behaviors of Lanzhou ice-saturated frozen silt under conventional triaxial compression (CTC) tests are simulated using the models.

5.1. Numerical aspects

To implement the proposed associated/nonassociated multiscale friction-damage coupled models into Abaqus®, we take advantage of the given user subroutine UMAT, where the values of stresses and solution-dependent state variables at the end of the increment must be updated, and the material Jacobian matrix must be provided for the mechanical constitutive model. For this purpose, one needs to ascertain the increment macroscopic stress-strain relation with the consistent tangent operator and subsequently develop the local integration algorithm of the established models.

5.1.1. Consistent tangent operator

From the computational standpoint and to model the strain-softening behavior of materials, plasticity-damage coupling problems have to be treated by following a strain-controlled procedure. The increment relationship of macroscopic stress versus macroscopic strain can be gained by differentiating Eq. (14) and followed

$$\dot{\boldsymbol{\Sigma}} = \mathbb{C}_{\text{tan}} : \dot{\boldsymbol{E}}. \tag{43}$$

where $\mathbb{C}_{\text{tan}}$ is the consistent tangent operator. The expression of $\mathbb{C}_{\text{tan}}$ can be ascertained by using the friction and damage consistency conditions.

In the generalized plasticity theory, the loading/unloading conditions illustrated in Kuhn-Tucker form are

$$\lambda^p \geq 0,\ \mathcal{F}\left(\boldsymbol{\Sigma}^c\right) \leq 0,\ \lambda^p \dot{\mathcal{F}}\left(\boldsymbol{\Sigma}^c\right) = 0. \tag{44}$$

It follows the condition

$$\lambda^p \dot{\mathcal{F}} = 0. \tag{45}$$

Accordingly, when material is under loading, if $\lambda^p \neq 0$, one has $\dot{\mathcal{F}} = 0$, i.e.,

$$\dot{\mathcal{F}} = \frac{\partial \mathcal{F}}{\partial \boldsymbol{E}} : \dot{\boldsymbol{E}} + \frac{\partial \mathcal{F}}{\partial \boldsymbol{E}^p} : \dot{\boldsymbol{E}}^p + \frac{\partial \mathcal{F}}{\partial d}\dot{d} = 0. \tag{46}$$

As far as damage is concerned, the consistency condition reads

$$\dot{\mathcal{D}} = \frac{\mathcal{D}}{\partial \boldsymbol{E}^p} : \dot{\boldsymbol{E}}^p + \frac{\partial \mathcal{D}}{\partial d}\dot{d} = 0. \tag{47}$$

- For the associated local plastic flow rule, the combinations of Eqs. (46) and (47) and by recalling that $\dot{\boldsymbol{E}}^p = \lambda^p \boldsymbol{N}_a$ and $\dot{d} = \lambda^d$, the nonnegative multipliers $\left(\lambda^p, \lambda^d\right)$ are determined as

$$\begin{cases} \lambda^p = \frac{1}{H_a} \frac{\partial \mathcal{F}}{\partial \boldsymbol{E}} : \dot{\boldsymbol{E}} \\ \\ \lambda^d = -\frac{\frac{\partial \mathcal{D}}{\partial \boldsymbol{E}^p} : \boldsymbol{N}_a}{\frac{\partial \mathcal{D}}{\partial d} H_a} \frac{\partial \mathcal{F}}{\partial \boldsymbol{E}} : \dot{\boldsymbol{E}} \end{cases} \tag{48}$$

  with hardening modulus $H_a = \frac{\partial \mathcal{F}}{\partial d}\frac{\partial \mathcal{D}}{\partial \boldsymbol{E}^p} : \boldsymbol{N}_a \frac{\partial \mathcal{D}}{\partial d} - \frac{\partial \mathcal{F}}{\partial \boldsymbol{E}^p} : \boldsymbol{N}_a$.

  By substituting Eqs.(48) into the differentiated form of Eq. (14), the consistent tangent operator $\mathbb{C}_{\text{tan}}$ reads

$$\mathbb{C}_{\text{tan}} = \begin{cases} \mathbb{C}_s, & \text{if } \mathcal{F}\left(\boldsymbol{\Sigma}^c\right) < 0 \\ \\ \mathbb{C}_s - \frac{1}{H_a}\left(\mathbb{C}_s : \boldsymbol{N}_a\right) \otimes \left(\boldsymbol{N}_a : \mathbb{C}_s\right), & \text{if } \mathcal{F}\left(\boldsymbol{\Sigma}^c\right) = 0 \end{cases}. \tag{49}$$

  $\mathbb{C}_{\text{tan}}$ in this case is symmetric, which provides a sound convenience for numerical application.

- For the nonassociated local plastic flow rule, using Eq. (46) and Eq. (47) and recalling that $\dot{\boldsymbol{E}}^p = \lambda^p \boldsymbol{N}_n$ and $\dot{d} = \lambda^d$, the nonnegative multipliers $\left(\lambda^p, \lambda^d\right)$ are obtained as

$$\begin{cases} \lambda^p = \frac{1}{H_n} \frac{\partial \mathcal{F}}{\partial \boldsymbol{E}} : \dot{\boldsymbol{E}} \\ \\ \lambda^d = -\frac{\frac{\partial \mathcal{D}}{\partial \boldsymbol{E}^p} : \boldsymbol{N}_n}{\frac{\partial \mathcal{D}}{\partial d} H_n} \frac{\partial \mathcal{F}}{\partial \boldsymbol{E}} : \dot{\boldsymbol{E}} \end{cases} \tag{50}$$

with hardening modulus $H_n = \frac{\partial \mathcal{F}}{\partial d}\frac{\partial \mathcal{D}}{\partial \boldsymbol{E}^p} : \boldsymbol{N}_a \frac{\partial \mathcal{D}}{\partial d} - \frac{\partial \mathcal{F}}{\partial \boldsymbol{E}^p} : \boldsymbol{N}_n$.

Similarity, by substituting Eqs.(50) into the differentiated form of Eq. (14), we obtain the consistent tangent operator

$$\mathbb{C}_{\text{tan}} = \begin{cases} \mathbb{C}_s, & \text{if } \mathcal{F}\left(\boldsymbol{\Sigma}^c\right) < 0 \\ \\ \mathbb{C}_s - \frac{1}{H_n}\left(\mathbb{C}_s : \boldsymbol{N}_n\right) \otimes \left(\boldsymbol{N}_a : \mathbb{C}_s\right), & \text{if } \mathcal{F}\left(\boldsymbol{\Sigma}^c\right) = 0 \end{cases} \tag{51}$$

In this case, $\mathbb{C}_{\text{tan}}$ exhibits nonsymmetry due to the nonassociated evolution laws (25).

5.1.2. Semi-implicit local numerical algorithm

The implicit return mapping algorithm proposed by Simo and Taylor (1985) has been extensively applied to solve elastoplastic problems. Nevertheless, to the authors' knowledge, this implicit algorithm is rarely used to solve the elastoplastic damage coupled model. Here, a semi-implicit return mapping method, which was proposed by Zhu et al. (2016a), has been developed for the associated/nonassociated multiscale models. Like the implicit return algorithm, the proposed semi-implicit return mapping algorithm has two steps. The elastic prediction and uncoupled plasticity-damage correction instead of the plasticity-damage coupled correction. The correction step is simple, and it involves freezing the damage variable when correcting the plasticity and fixing the plasticity when correcting the damage. A geometrical illustration of this algorithm, including strain hardening and strain softening, is depicted in Figure 6. For a strain increment $\dot{\boldsymbol{E}}_{i+1}$ from the global iteration in Abaqus®, one can obtain the current strain tensor as $\boldsymbol{E}_{i+1} = \boldsymbol{E}_i + \dot{\boldsymbol{E}}_{i+1}$. Freezing $d_{i+1} = d_i$ and assuming that the strain increment $\dot{\boldsymbol{E}}_{i+1}$ is completely elastic, i.e., $\boldsymbol{E}^p_{i+1} = \boldsymbol{E}^p_i$. The macroscopic stress is predicted as follows:

$$\boldsymbol{\Sigma}^{\text{trial}}_{i+1} = \mathbb{C}_s : \left(\boldsymbol{E}_{i+1} - \boldsymbol{E}^p_i\right). \tag{52}$$

Next, check the plastic criterion $\mathcal{F}^{\text{trial}}_{i+1}\left(\boldsymbol{\Sigma}^c\right)$. If $\mathcal{F}^{\text{trial}}_{i+1}\left(\boldsymbol{\Sigma}^c\right) \leq 0$, then $\dot{\boldsymbol{E}}^p_{i+1} = \boldsymbol{0}$ and $\dot{d}_{i+1} = 0$; otherwise $\dot{\boldsymbol{E}}^p_{i+1} \neq \boldsymbol{0}$ and $\dot{d}_{i+1} \neq 0$. In the latter case, we employ the uncoupled plasticity-damage correction procedure. Here, the superscript j ($j = 1, \ldots, m_{iter}$ with $m_{iter} = 500$) is used for the inner iteration process (related to a correction procedure). For clarity, we omit the loading subscript $i + 1$ during the correction process.

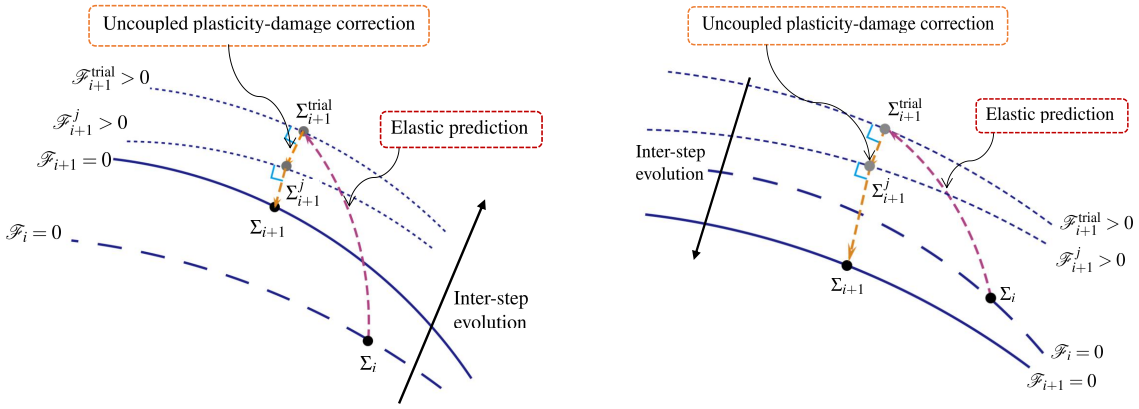

(a) Strain hardening (b) Strain softening

Figure 6: Geometrical illustration of the semi-implicit return mapping algorithm

First, we explicitly determine the plastic multiplier with damage frozen in its previous state. For a monotonic loading, when $\mathcal{F}^j\left(\boldsymbol{E}^{p,j}\right) > 0$ during elastic prediction, one should have $\mathcal{F}^{j+1}\left(\boldsymbol{E}^{p,j} + \delta\boldsymbol{E}^{p,j}\right) = 0$. Using the first-order Taylor expansion, the friction criterion is linearized as follows:

$$\mathcal{F}^{j+1} = \mathcal{F}^j + \frac{\partial \mathcal{F}^j}{\partial \boldsymbol{E}^{p,j}} : \delta\boldsymbol{E}^{p,j} \approx 0. \tag{53}$$

By using the normality flow rule (22) for the associated case with $\boldsymbol{N} = \boldsymbol{N}_a$ or using (25) for the nonassociated case with $\boldsymbol{N} = \boldsymbol{N}_n$, one has

$$\mathcal{F}^{j+1} = \mathcal{F}^j + \delta\lambda^{p,j}\frac{\partial \mathcal{F}^j}{\partial \boldsymbol{E}^{p,j}} : \boldsymbol{N}^j \approx 0, \tag{54}$$

from which one can derive the plastic multiplier

$$\delta\lambda^{p,j} = -\frac{\mathcal{F}^j}{\frac{\partial \mathcal{F}^j}{\partial \boldsymbol{E}^{p,j}} : \boldsymbol{N}^j}. \tag{55}$$

Accordingly, the plastic strain is updated

$$\boldsymbol{E}^{p,j+1} = \boldsymbol{E}^{p,j} + \delta\lambda^{p,j}\,\boldsymbol{N}^j. \tag{56}$$

Next, if damage criterion $\mathcal{D}^j\left(\boldsymbol{E}^{p,j+1}, d^j\right) \le 0$, then $d^{j+1} = d^j$. Otherwise, $\mathcal{D}^j\left(\boldsymbol{E}^{p,j+1}, d^j\right) > 0$, we assume that $\mathcal{D}^j\left(\boldsymbol{E}^{p,j+1}, d^j + \delta d^j\right) = 0$. Similarly, the damage criterion can be linearized as

$$\mathcal{D}^{j+1} = \mathcal{D}^j + \delta\lambda^{d,j}\frac{\partial \mathcal{D}^j}{\partial d^j} \approx 0 \tag{57}$$

Then, the damage multiplier is

$$\delta\lambda^{d,j} = -\frac{\mathcal{D}^j}{\frac{\partial \mathcal{D}^j}{\partial d^j}}. \tag{58}$$

The damage variable is updated

$$d^{j+1} = d^{j} + \delta\lambda^{d,j}. \tag{59}$$

Finally, the macroscopic stress is updated as:

$$\boldsymbol{\Sigma}^{j+1} = \mathbb{C}_s : \left(\boldsymbol{E} - \boldsymbol{E}^{p,j+1}\right). \tag{60}$$

The local iteration process ends if specific tolerances are reached ($\left|\mathcal{F}^{j+1}\right| \leq \epsilon_{\text{local}}$.)

For clarity, we give the flowchart for the semi-implicit local numerical algorithm, as shown in Algorithm 1

5.2. Associated multiscale friction-damage model validation

5.2.1. Parameter calibration procedure

For numerical simulation, a crucial step is to calibrate the model parameters. The associated multiscale model has only nine parameters, and all of them have clear physical mechanisms:

- Elastic modulus E_i and Poisson's ratio ν_i of the ice crystals. One obtains these two material parameters from the pre-peak linear elastic part of stress-strain curves of ice samples under CTC tests. These two parameters are significantly affected by temperature (Zhu et al., 2010b), especially the elastic modulus E_i.

- Elastic modulus E_m and Poisson's ratio ν_m of mineral grains. Similarly, one can obtain these two material parameters from the linear part of the stress-strain curves of saturated unfrozen silt under drained conditions (Zhang et al., 2019a).

- Plastic and damage parameters (α, η_c, b, $\mathcal{R}_c$, d_c) in mesoscale controlling the strength and plastic deformation of frozen silt. Parameters b, η_c and $\mathcal{R}_c$ are associated with the stress at peak strength state, which can be calibrated by optimally fitting the test strength envelope using the strength criterion (37). Parameter α controls the initial friction coefficient η, which corresponds to the initial yield stress. Parameter d_c is the critical damage value related to the peak strength state, which controls the damage kinetics for both pre-and post-peak stress stages. The sensitive analysis of parameters d_c and α is illustrated in Section 5.2.2.

5.2.2. Model simulation Lanzhou frozen silt

For validation, the CTC test data for comparison were extracted from Zhang et al. (2018b). The tested silt was taken from Lanzhou, and primary physical parameters were illustrated in Table 1. Zhang et al. (2018b) prepared the test specimens with saturation greater than 95% as cylinders with 12.5 cm in height and 6.18 cm in diameter. To guarantee that the tested frozen silt was in an ice-saturated state, the specimens were quickly frozen and subsequently placed into a triaxial

Algorithm 1: Flowchart of the semi-implicit local numerical algorithm

Input: $\dot{\boldsymbol{E}}_{i+1}, \boldsymbol{\Sigma}_i, \boldsymbol{E}_i, d_i, \boldsymbol{E}_i^p, \mathbb{C}_m, \mathbb{C}_i, \varphi_i$

Output: $\boldsymbol{\Sigma}_{i+1}, \boldsymbol{E}_{i+1}, d_{i+1}, \boldsymbol{E}_{i+1}^p, \mathbb{C}_s, \mathbb{C}_{\tan}$

Calculate $\mathbb{C}_s$ using Eq. (2), and compute Q_1, Q_2, $\varkappa_1$ and $\varkappa_2$;

Elastic prediction:

$\boldsymbol{E}_{i+1} = \boldsymbol{E}_i + \dot{\boldsymbol{E}}_{i+1}$; $\boldsymbol{\Sigma}_{i+1}^{\text{trial}} = \mathbb{C}_s : \left(\boldsymbol{E}_{i+1} - \boldsymbol{E}_i^p\right)$

if $\mathcal{F}_{i+1}\left(\boldsymbol{\Sigma}^c\right) \leq 0$ **then**

  $\dot{\boldsymbol{E}}_{i+1}^p = \boldsymbol{0}$ and $\dot{d}_{i+1} = 0$;

  $d_{i+1} = d_i$; $\boldsymbol{E}_{i+1}^p = \boldsymbol{E}_i^p$; $\mathbb{C}_{i+1}^{\tan} = \mathbb{C}_s$

else

  Uncoupled plasticity-damage correction:

  for $j = 1 \ldots m_{iter}$ **do**

    Calculate the plastic multiplier $\delta\lambda^{p,j}$ by using Eq. (55) or Eq. (25);

    Update $\boldsymbol{E}^{p,j+1} = \boldsymbol{E}^{p,j} + \delta\lambda^{p,j}\boldsymbol{N}^j$;

    if $\mathcal{D}^j\left(\boldsymbol{E}^{p,j+1}, d^j\right) \geq 0$ **then**

      Caluclate the increment of the damage multiplier $\delta\lambda^{d,j}$ by using Eq. (58)

    else

      $\delta\lambda^{d,j} = 0$.

    Update $d^{j+1} = d^j + \delta\lambda^{d,j}$, η^{j+1} and $\boldsymbol{N}^{j+1}$ by using Eq. (21) and (23) (or Eq. (25));

    if $\left|\mathcal{F}^{j+1}\right| \leq \epsilon_{local}$ **then**

      Return;

    else

      $j = j + 1$

  $\mathbb{C}_{\tan} = \mathbb{C}_s - \frac{1}{H_a}\left(\mathbb{C}_s : \boldsymbol{N}_a\right) \otimes \left(\boldsymbol{N}_a : \mathbb{C}_s\right)$ for the associated case,

  and $\mathbb{C}_{\tan} = \mathbb{C}_s - \frac{1}{H_n}\left(\mathbb{C}_s : \boldsymbol{N}_n\right) \otimes \left(\boldsymbol{N}_a : \mathbb{C}_s\right)$ for the nonassociated case;

  $\boldsymbol{\Sigma}^{j+1} = \mathbb{C}_s : \left(\boldsymbol{E} - \boldsymbol{E}^{p,j+1}\right)$;

pressure cell of MTS low-temperature testing machine at a given temperature (kept constant for 24 h). The testing confining pressures Σ_3 were 0.3-15.0 MPa under temperatures -6, -10 and -15°C. For more details, one can refer to the work of (Zhang et al., 2018b,a).

Table 1: Basic physical parameters of Lanzhou silt (Zhang et al., 2018b)

Dry density ρ_m (g/cm^3)	Relative density (g/cm^3)	Plastic limit(%)	Liquid limit (%)	Saturated water content ω_{sa} (%)
1.54	2.69	19.4	27.6	27.8

When water freezes into ice crystals, it increases in volume by one-ninth. In this case, for the ice-saturated frozen silt, the volume of crystal ice $\Omega_i = \Omega_m \rho_m \omega_{sa} \times \left(1 + \frac{1}{9}\right)$, where Ω_m, ρ_m and ω_{sa} are volume of mineral grains, dry density and saturated water content of silt, respectively. Using the second term of Eq. (1) and physical parameters of Lanzhou silt in Table 1, one obtains $\varphi_i = 0.322$. Based on the works of Zhu et al. (2010b), Chang et al. (2019), Zhang et al. (2018b), the elastic parameters of ice crystals and mineral grains are shown in Table 2. Once elastic parameters (E_i, ν_i, E_m, ν_m) and the volume fraction of ice crystals have been determined, the bulk modulus k_s and shear modulus μ_s are estimated using Eq. (3); then, Q_1, Q_2, $\varkappa_1$ and $\varkappa_2$ can be easily calculated.

Table 2: Elastic parameters of ice crystals and mineral grains

Parameters	E_i (MPa)	ν_i	E_m (MPa)	ν_m
Values	$\frac{7772.3\|T\|}{1.1746+\|T\|}$	0.3	120	0.25

Now, we focus on determining the plastic and damage variables for Lanzhou frozen silt. Based on the test data from Zhang et al. (2018b), we can obtain the relationship between mean macroscopic stress Σ_m and deviatoric macroscopic stress Σ_d under different temperatures, as illustrated in Figure 7(a). The nonlinear strength criterion (37) was fitted to the test data using a nonlinear minimum least square subroutine Lsqcurvefit from MATLAB. Parameters η_c, b and $\mathcal{R}_c$ are shown in Table 3, and the corresponding fitting curves are illustrated in Figure 7(a). The associated macroscopic strength criterion fits the test data well and can be considered suitable for Lanzhou frozen silt; all regression R^2 coefficients exceed 0.979. The strength envelopes of Lanzhou frozen silt

under different temperatures are also constructed in the three-dimensional principal stress space. As shown in Figure 7(b), the failure surfaces are shaped as long ladles with circular cross-sections.

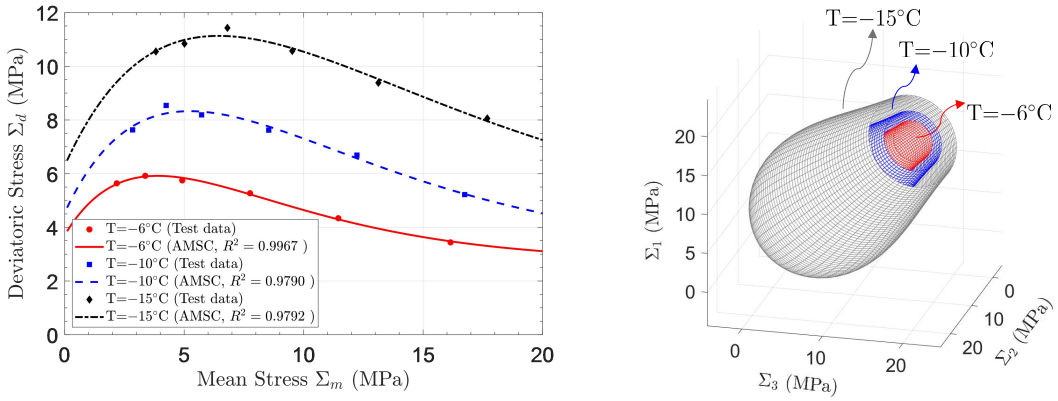

(a) (b)

Figure 7: Strength prediction of Lanzhou frozen silt. (a) Comparison of the associated macroscopic strength criterion ((37)) predictions and test data of frozen silt under different temperatures in $\Sigma_m - \Sigma_d$ plane. Solid points are test data extracted from Zhang et al. (2018b), (b) Failure surfaces of the associated macroscopic strength criterion ((37)) in three-dimensional principal stress space under different temperatures.

Table 3: Plastic and damage parameters for Lanzhou frozen silt under different temperatures

T (°C)	η	b	$\mathcal{R}_c$	α
-6	1.54	0.023	0.02	$\frac{1}{3}$
-10	1.92	0.017	0.024	$\frac{1}{2}$
-15	2.03	0.014	0.042	$\frac{2}{3}$

Figure 8 shows the strength envelopes in the $\Sigma_m - \Sigma_d$ plane with the variation of η_c, b and $\mathcal{R}_c$. In Figure 8(a), η_c controls the initial slope of the strength envelope and influences the intercept of the strength envelope. Specifically, with increasing η_c, Σ_d^0 and Σ_d increase, but it has no influence on the residual strength Σ_d^{res}. Figure 8(b) shows that parameter b controls the degradation rate friction coefficient η. With increasing b, the critical mean stress Σ_d and maximum deviatoric stress Σ_d^{max} decrease. In Figure 8(c), the evolutions of strength curves are presented by varying maximum

damage resistance $\mathcal{R}_c$ from 0.005 to 0.04. $\mathcal{R}_c$ plays a significant role of the strength. Logically, Σ_d^0, Σ_d^{max} and Σ_d^{res} increase when $\mathcal{R}_c$ increases.

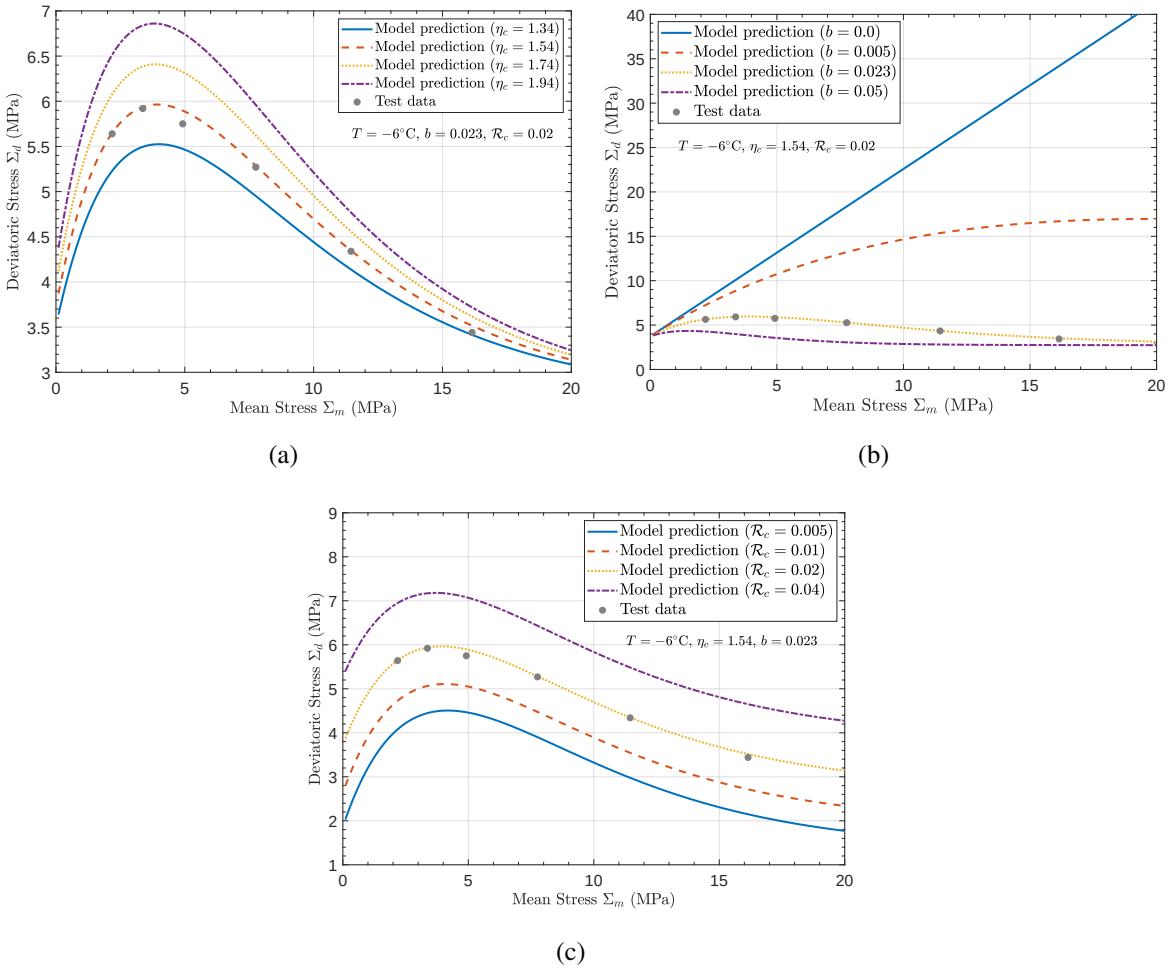

Figure 8: Strength curves in the meridian plane with the variation of (a)η_c, (b) b and (c)$\mathcal{R}_c$

Parameter α and critical damage d_c remain to be determined. The results of parametric studies by varying their values are presented in Figures 9 and 10. Parameter α controls the initial value friction coefficient and initial yield point in the stress-strain curves (Figure 9). With this rule and by analyzing the test data extracted from Zhang et al. (2018b), for simplicity, we take α as a constant for a given temperature (listed in Table 3). In Figure 10, d_c plays a role in controlling the inelastic strains at peak stress and the evolution rate of the friction coefficient. More precisely, with increasing d_c, the total inelastic strains at peak stress and evolution rate of friction coefficient increase, while d_c does not affect the peak stress and maximum value of friction coefficient. To obtain a better fit to the test data, the critical damage d_c can be considered the logistic function of

the confining pressure:

$$d_c\left(\Sigma_3\right)=\frac{d_c^0 e^{r\Sigma_3}}{1+d_c^0\left(e^{r\Sigma_3}-1\right)} \tag{61}$$

where d_c^0 is the initial value of d_c corresponding $\Sigma_3 = 0$, and r controls the evolution rate of d_c. These two parameters under different temperature are obtained using the Cftool (Curve Fitting Tool) toolbox in Matlab and are shown in Figure 11.

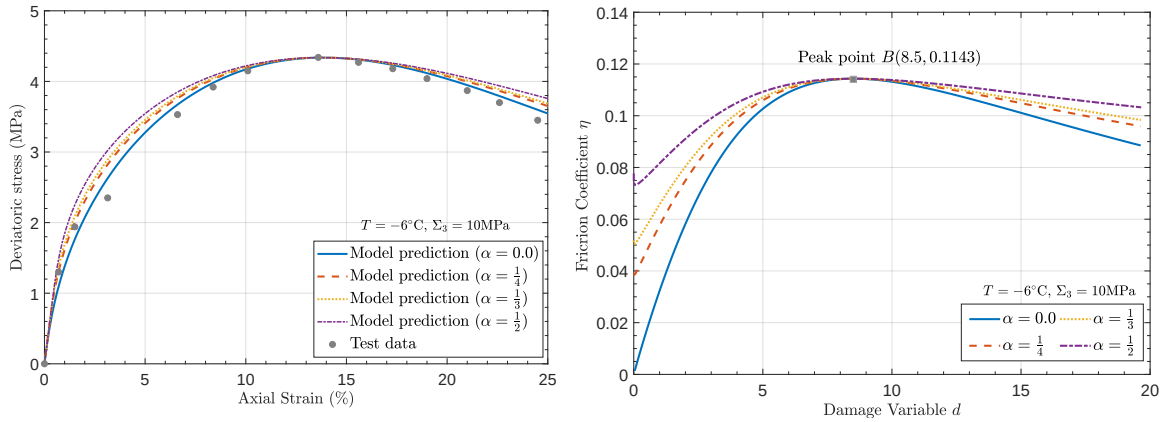

(a) Deviatoric stress- Axial strain (b) Friction coefficent evolution

Figure 9: Sensitivity analyses of parameter α using CTC tests with $\Sigma_3 = 10$ MPa and $T = -6°C$

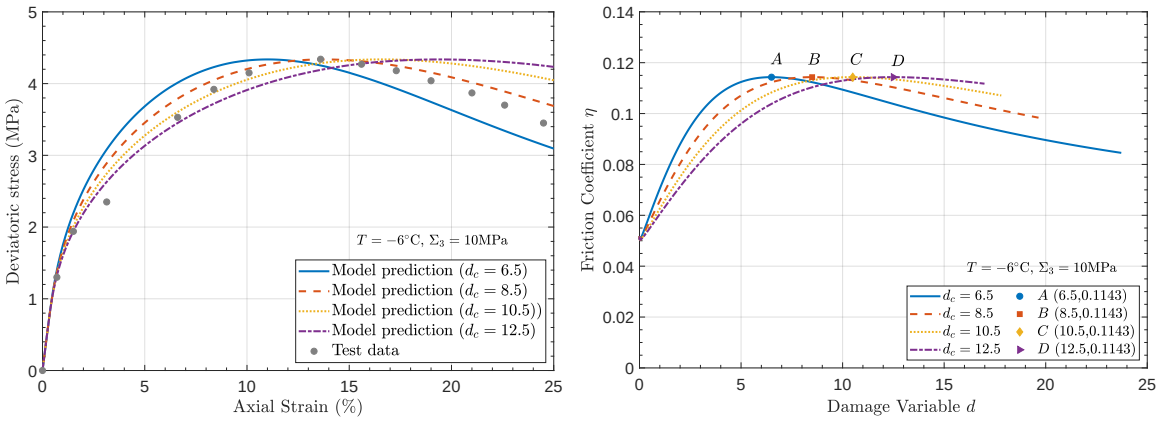

(a) Deviatoric stress- Axial strain (b) Friction coefficent evolution

Figure 10: Sensitivity analyses of parameter d_c using CTC tests with $\Sigma_3 = 10$ MPa and $T = -6°C$

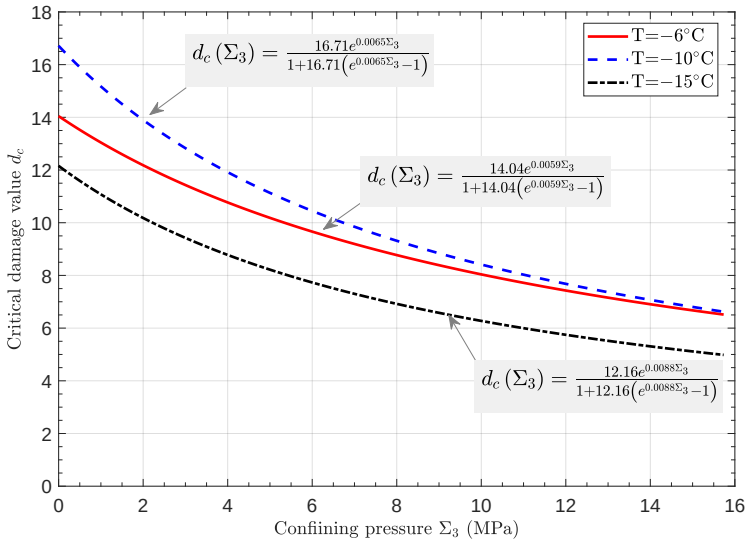

Figure 11: Describing the evolution of parameter d_c with increasing confining pressure under different temperatures by using logistic function (61)

The CTC tests under different temperatures were simulated with the determined parameters by utilizing the proposed associated multiscale model. Figure 12(a) shows the comparisons between model simulations and test data on macroscopic deviatoric stress-axial strain curves under different confining pressures (Σ_3=0.3, 1.4, 3.0, 6.0, 10.0 and 15.0 MPa) at the temperature of −6°C. The simulated results can well reproduce the axial deformation and stress features of the frozen silt under different confining pressures, while the volumetric strain cannot be reproduced by the proposed model (Figure 12(b)). The reason may be the use of the associated local plastic flow rule. Figure 12(c) illustrates the evolution of the friction coefficient. The friction coefficient decreases with the increase in confining pressure.

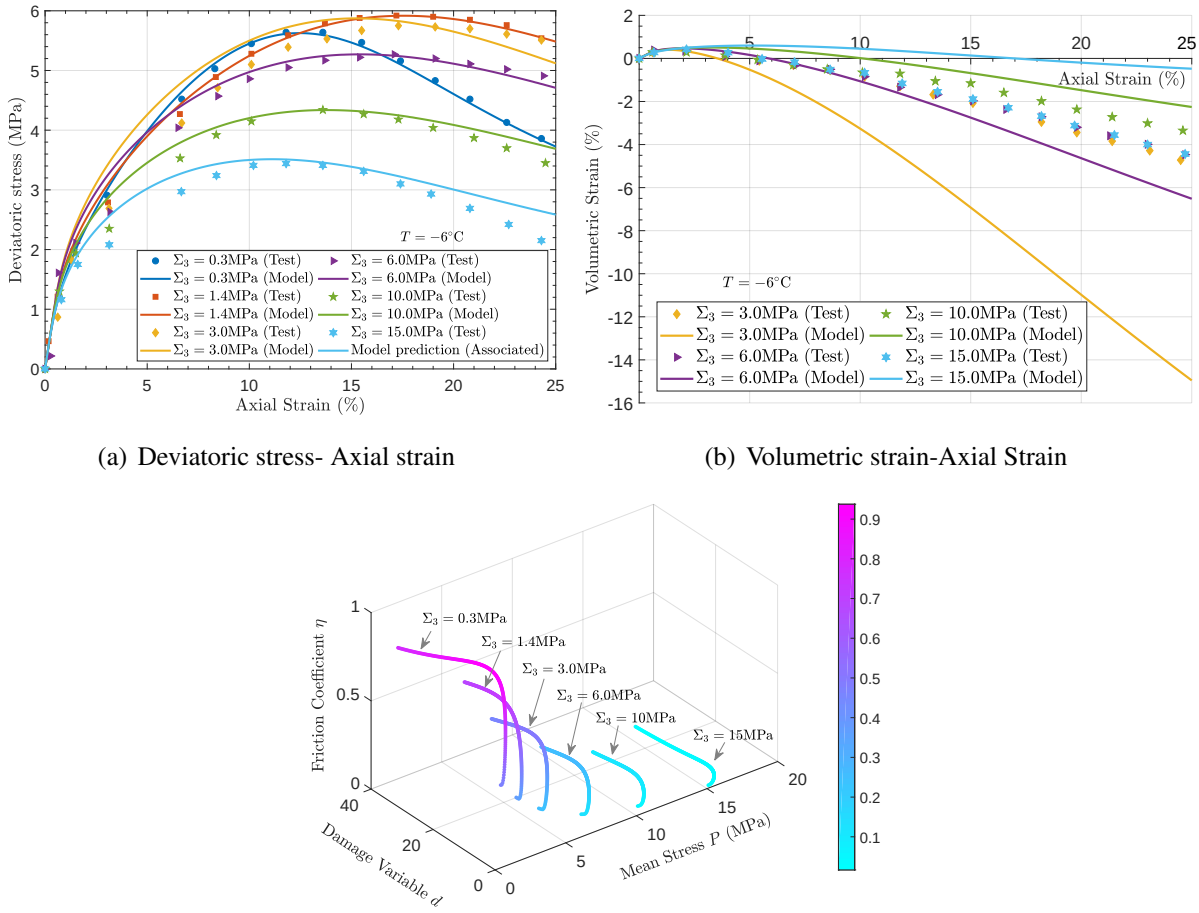

(a) Deviatoric stress- Axial strain

(b) Volumetric strain-Axial Strain

(c) Friction coefficient evolution

Figure 12: Associated multiscale model simulations of frozen silt mechanical behaviors with CTC tests under −6°C (test data extracted from Zhang et al. (2018b))

Furthermore, Figure 13 shows the associated multiscale model simulations on the stress-strain relation at the temperature of −10°C and −15°C. The model simulations and test data well coincide with each other under a large range of confining pressures. Thus, the proposed associated multi-scale model can accurately reproduce the influences of the temperature and confining pressures on the axial strain and stress properties of frozen silt.

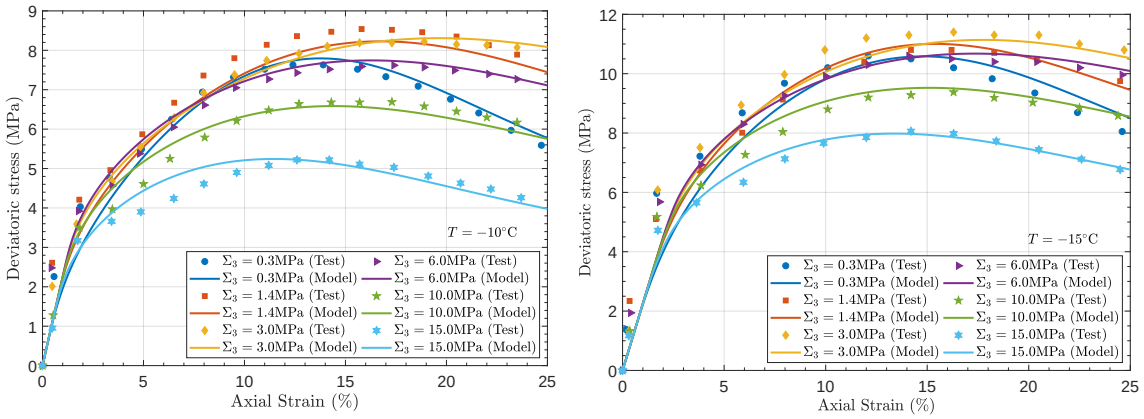

(a) T=-10°C (b) T=-15°C

Figure 13: Comparisons between the associated multiscale model predictions and test data on stress-axial strain behaviors under −10°C and −15°C (test data extracted from Zhang et al. (2018b))

5.3. Nonassociated multiscale friction-damage model validation

In this subsection, the accuracy of the nonassociated multiscale model is assessed. The parameter identification procedure proposed in Section5.2.1 is also valid for the nonassociated model. Accordingly, one can calibrate ten parameters in the nonassociated multiscale model from CTC tests on Lanzhou frozen silt at the temperature of −6°C (Zhang et al., 2018b). Here, we take $\kappa = 0.2$. The values of parameters $\eta_c = 1.59$, $b = 0.025$ and $\mathcal{R}_c = 0.023$ are obtained by fitting the strength envelope with Eq. (42). Figure 14 compares the strength criterion with associated and nonassociated local plastic flow rule fits and test data of frozen silt at the temperature of −6°C. Both strength criteria (37) and (42) well reproduce the strength properties of the frozen silt. The other parameters in the nonassociated multiscale model are taken to be equal to those in the associated multiscale model in section 5.2.2.

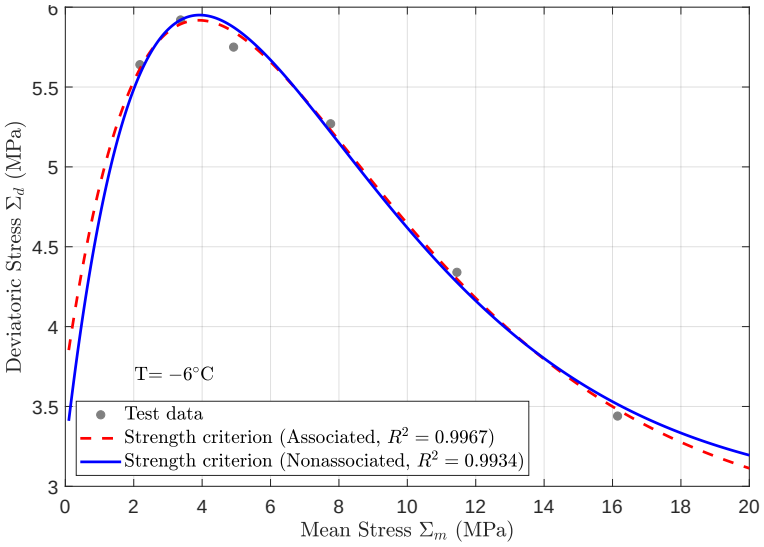

Figure 14: Comparison between the associated strength criterion (37) and the nonassociated strength criterion (42) fits to the test data of frozen silt at the temperature of −6°C (test data extracted from Zhang et al. (2018b))

Figure 15 shows the multiscale models simulations (associated and nonassociated) of Lanzhou frozen silt properties under CTC tests (Σ_3 = 3, 6, 10, and 15 MPa) and compares them with test data. Both associated and no-associated multiscale model simulations are consistent with the test data for the axial strain. The nonassociated multiscale model better describes the transition from volumetric compressibility to dilation with the increase in deviatoric stress, which demonstrates a great advancement over the predictions of the associated multiscale model.

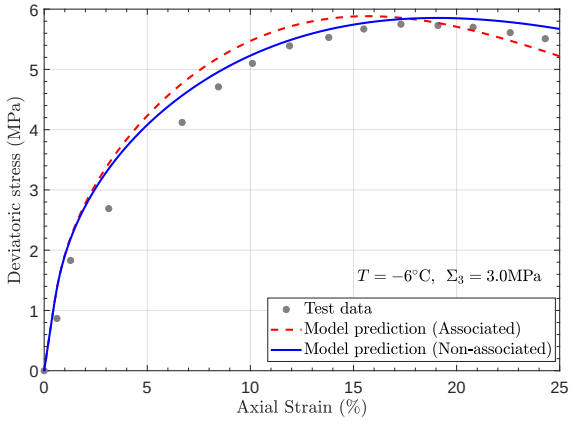

(a) Σ_3 = 3 MPa

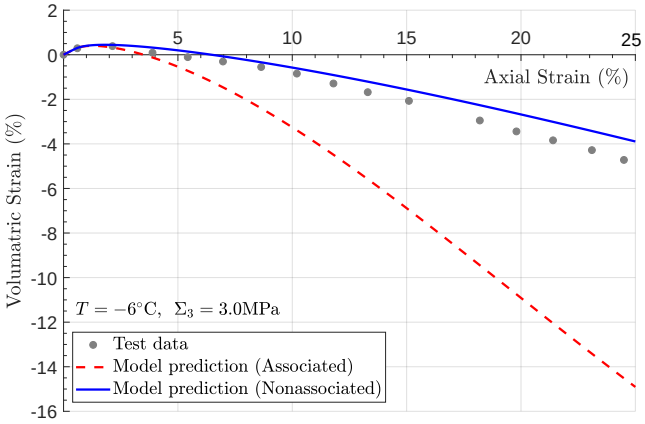

(b) Σ_3 = 3 MPa

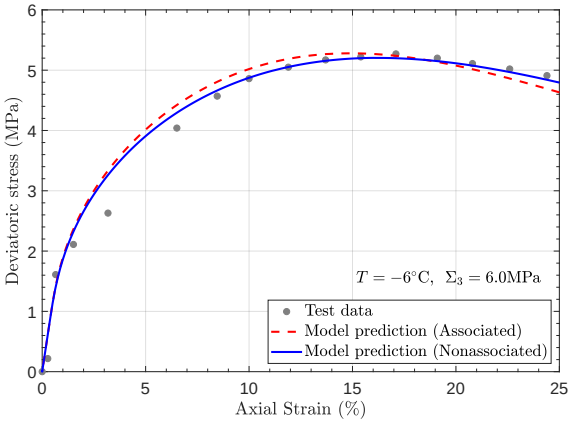

(c) Σ_3 = 6 MPa

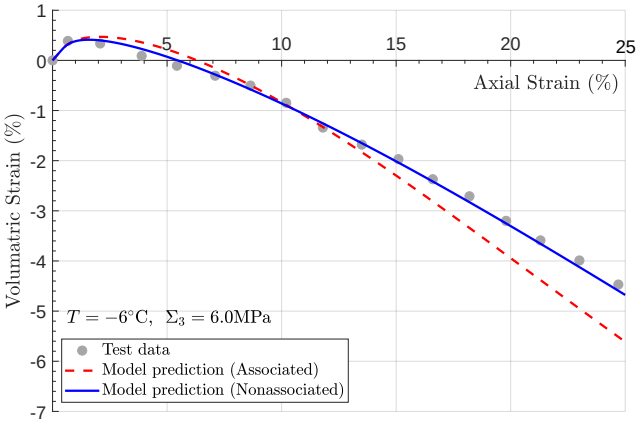

(d) Σ_3 = 6 MPa

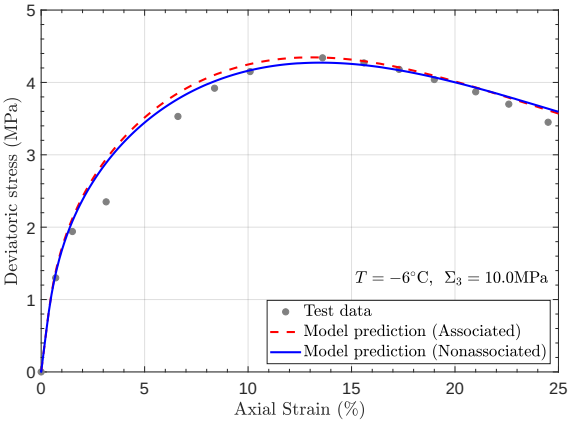

(e) Σ_3 = 10 MPa

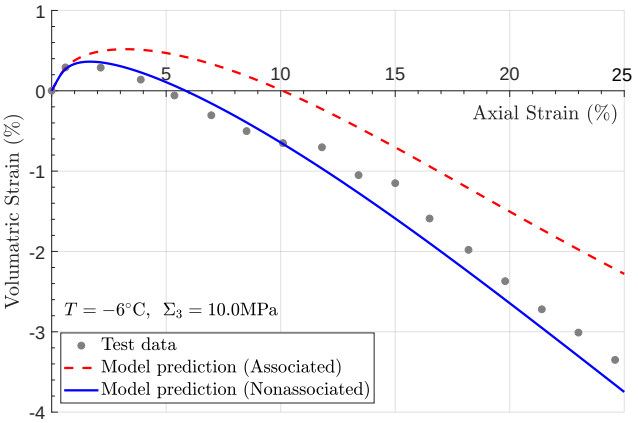

(f) Σ_3 = 10 MPa

Figure 15: Comparisons of multiscale models (associated and nonassociated) simulations and test data of CTC tests under different confining pressures at $-6°C$

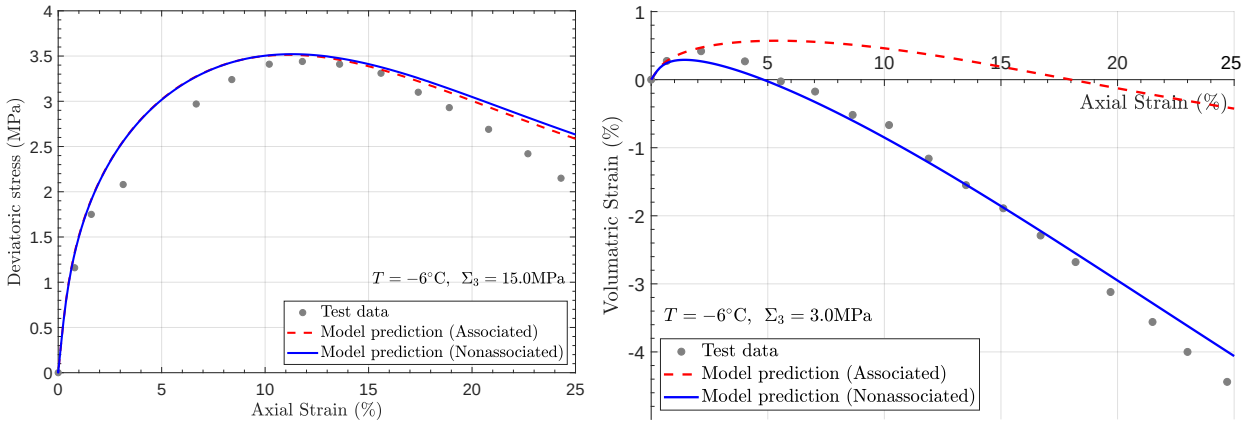

(a) Σ_3 = 15 MPa (b) Σ_3 = 15 MPa

Figure 15: (continued)

6. Conclusions

In this work, physical multiscale friction-damage coupled models and nonlinear strength criteria of ice-saturated frozen silt have been proposed based on linear homogenization theory. The studied material contains mesocracks embedded in a frozen silt matrix at mesoscale. The frozen silt matrix itself is composed of elastic mineral practices and elastic crystal ice inclusion. With this microstructure, the effective elastic behaviors of frozen silt are obtained with a two-step linear Mori-Tanaka homogenization scheme. The plastic deformation is due to the frictional sliding along mesocracks, while the damage evolution is related to the initiation and propagation of mesocracks. By incorporation the thermodynamics framework and Mori-Tanka homogenization procedure, we have derived the macroscopic stress-strain relations and thermodynamics forces associated with plastic strain and damage. The frictional sliding is driven by the local stress tensor applied onto mesocracks, which is affected by the damage state. The propagation of mesocracks controls the damage evolution. Therefore, these two inelastic processes are inherently coupled. The evolution of damage and plasticity are described by an energy release damage and a frictional sliding criterion with an associated/nonassociated local plastic flow rule, respectively. In particular, the effect of pressure melting and damage evolution on the variation of surface asperities of mesocracks has been considered. With the aid of friction-damage coupled analysis, associated/nonassociated macroscopic nonlinear strength criteria are derived.

For numerical implementation, a semi-implicit local numerical algorithm for the proposed associated/nonassociated multiscale models was developed. Then, parameter calibration procedures from CTC tests were developed. The accuracy of associated/nonassociated multiscale models and associated/nonassociated strength criteria were verified through a comprehensive campaign

of comparisons on Lanzhou frozen silt in CTC tests under an amount of confining pressure with different temperatures. Remarkable consistency was obtained between predicted results and test axial strains and strengths for the associated multiscale model and strength criterion. Nevertheless, the associated multiscale model could not correctly reproduce the experimental volumetric strains. The nonassociated multiscale model can reproduce the primary mechanical behavior of the frozen silt to account for its microstructure evolution.

Compared with most previous micro-mechanics-based models devoted to geological materials, the main advantage of the present model is to incorporate precise physical mechanisms and specific microstructural evolution of frozen soil. However, in the present work, we only focus on the time-independent mechanical behaviors of ice-saturated frozen silt. This work should be extended to consider both instantaneous and time-dependent behaviors of fully and partially saturated frozen silt. Moreover, the practical application of the proposed models to permafrost engineering problems is also being conducted in our ongoing work.

Acknowledgments

This study was jointly supported by the National Natural Science Foundation of China (Grant No. 42001053), the Guangdong Basic and Applied Basic Research Foundation (Grant No. 2019A1515110626), the National Key RD Program of China (Grant No. 2017YFC1501100), the Second Tibetan Plateau Scientific Expedition and Research (STEP) program (Grant No. 2019QZKK0905), China Post-doctoral Science Foundation funded projects (Nos. 2020M682707, 2021T140219) and the National Program on Key Basic Research Projects of China (No. 2018YFC0809601).

References

Anderson, D. M., Morgenstern, N., 1973. Physics, chemistry and mechanics of frozen ground: A review. In: Proceedings of the Second International Conference on Permafrost. National Academy of Sciences Washington, DC, pp. 257–288.

Budiansky, B., O'connell, R. J., 1976. Elastic moduli of a cracked solid. International journal of Solids and structures 12 (2), 81–97.

Chang, D., Lai, Y. M., Zhang, M. Y., 2019. A meso-macroscopic constitutive model of frozen saline sandy soil based on homogenization theory. International Journal of Mechanical Sciences 159, 246–259.

Chang, X. X., Ma, W., Wang, D. Y., 2008. Study on the strength of frozen clay at high confining pressure. Frontiers of Earth Science in China 2 (2), 240–242.

Damiani, R., Sun, L. Z., 2017. Microstructural characterization and effective viscoelastic behavior of magnetorheological elastomers with varying acetone contents. International Journal of Damage Mechanics 26 (1), 104–118.

Dejaloud, H., Jafarian, Y., 2017. A micromechanical-based constitutive model for fibrous fine-grained composite soils. International Journal of Plasticity 89, 150–172.

Fish, A., 1991. Strength of frozen soil under a combined stress state. In: Proc. of 6th Int. Symp. on Ground Freezing. pp. 135–145.

French, H. M., 2017. The periglacial environment. John Wiley & Sons.
Jin, W. C., Arson, C., 2018. Micromechanics based discrete damage model with multiple non-smooth yield surfaces: Theoretical formulation, numerical implementation and engineering applications. International Journal of Damage Mechanics 27 (5), 611–639.
Krabbenhoft, K., Karim, M. R., Lyamin, A. V., Sloan, S. W., 2012. Associated computational plasticity schemes for nonassociated frictional materials. International Journal for Numerical Methods in Engineering 90.
Lai, Y. M., Jin, L., Chang, X. X., 2009. Yield criterion and elasto-plastic damage constitutive model for frozen sandy soil. International journal of plasticity 25 (6), 1177–1205.
Lai, Y. M., Liao, M. K., Hu, K., 2016. A constitutive model of frozen saline sandy soil based on energy dissipation theory. International Journal of Plasticity 78, 84–113.
Lai, Y. M., Xu, X. T., Dong, Y. H., Li, S. Y., 2013. Present situation and prospect of mechanical research on frozen soils in china. Cold Regions Science & Technology 87 (2), 6–18.
Lai, Y. M., Xu, X. T., Yu, W. B., Qi, J. L., 2014. An experimental investigation of the mechanical behavior and a hyperplastic constitutive model of frozen loess. International Journal of Engineering Science 84 (84), 29–53.
Lai, Y. M., Yang, Y. G., Chang, X. X., Li, S. Y., 2010. Strength criterion and elastoplastic constitutive model of frozen silt in generalized plastic mechanics. International Journal of Plasticity 26 (10), 1461–1484.
Liao, M. K., Lai, Y. M., Wang, C., 2016. A strength criterion for frozen sodium sulfate saline soil. Canadian Geotechnical Journal 53 (7), 1176–1185.
Liu, E. L., Lai, Y. M., Wong, H., Feng, J. L., 2018. An elastoplastic model for saturated freezing soils based on thermo-poromechanics. International Journal of Plasticity 107, 246–285.
Liu, X., Liu, E., Zhang, D., Zhang, G., Song, B., 2019a. Study on strength criterion for frozen soil. Cold Regions Science & Technology 161, 1–20.
Liu, X. Y., Liu, E. L., Zhang, D., Zhang, G., Yin, X., Song, B. T., 2019b. Study on effect of coarse-grained content on the mechanical properties of frozen mixed soils. Cold Regions Science & Technology 158, 237–251.
Liu, Z., 2005. A damage constitutive model for frozen soils under uniaxial compression based on ct dynamic distinguishing. Rock and Soil Mechanics 26 (4), 542–546.
Loria, A. F. R., Frigo, B., Chiaia, B., 2017. A non-linear constitutive model for describing the mechanical behaviour of frozen ground and permafrost. Cold Regions Science & Technology 133, 63–69.
Ma, W., Wu, Z. W., Zhang, C. Q., 1995. Strength and yield criteria of frozen soil. Progress in Natural Science:Materials International 4, 23–27.
Ma, W., Wu, Z. W., Zhang, L. X., Chang, X. X., 1999. Analyses of process on the strength decrease in frozen soils under high confining pressures. Cold Regions Science & Technology 29 (1), 1–7.
Mori, T., Tanaka, K., 1973. Average stress in matrix and average elastic energy of materials with misfitting inclusions. Acta metallurgica 21 (5), 571–574.
Nielsen, S., Toro, G. D., Griffith, W., 2010. Friction and roughness of a melting rock surface. Geophysical Journal International 182 (1), 299–310.
Ning, J. G., Wang, H., Zhu, Z. W., Sun, Y. X., 2005. Investigation of the constitutive modle of frozen soil based on meso-mechanics. Journal of Beijing Institute of Technology 25 (10), 847–1851.
Parameswaran, V. R., 1985. Effect of alternating stress on the creep of frozen soils. Mechanics of Materials 4 (2), 109–119.
Parameswaran, V. R., 1987. Extended failure time in the creep of frozen soils. Mechanics of Materials 6 (3), 233–243.
Qi, J. L., Ma, W., 2007. A new criterion for strength of frozen sand under quick triaxial compression considering effect of confining pressure. Acta Geotechnica 2 (3), 221–226.

Russo, G., Corbo, A., Cavuoto, F., Autuori, S., 2015. Artificial ground freezing to excavate a tunnel in sandy soil. measurements and back analysis. Tunnelling and Underground Space Technology 50, 226–238.

Shen, W. Q., Shao, J. F., 2018. A micro-mechanics-based elastic–plastic model for porous rocks: applications to sandstone and chalk. Acta Geotechnica 13 (2), 329–340.

Shen, W. Q., Shao, J. F., Oueslati, A., De Saxce, G., Zhang, J., 2018. An approximate strength criterion of porous materials with a pressure sensitive and tension-compression asymmetry matrix. International Journal of Engineering Science 132, 1–15.

Simo, J. C., Taylor, R. L., 1985. Consistent tangent operators for rate-independent elastoplasticity. Computer Methods in Applied Mechanics & Engineering 48 (1), 101–118.

Tounsi, H., Rouabhi, A., Tijani, M., Guérin, F., 2019. Thermo-hydro-mechanical modeling of artificial ground freezing: application in mining engineering. Rock Mechanics and Rock Engineering 52 (10), 3889–3907.

Wang, D. Y., Ma, W., Chang, X. X., 2004. Analyses of behavior of stress–strain of frozen lanzhou loess subjected to k0 consolidation. Cold regions science and technology 40 (1-2), 19–29.

Wu, Y., Ju, J. W., 2017. Elastoplastic damage micromechanics for continuous fiber-reinforced ductile matrix composites with progressive fiber breakage. International Journal of Damage Mechanics 26 (1), 4–28.

Yang, Y. G., Lai, Y. M., Li, J. B., 2010. Laboratory investigation on the strength characteristic of frozen sand considering effect of confining pressure. Cold Regions Science & Technology 60 (3), 245–250.

Yershov, E. D., 2004. General geocryology. Cambridge university press.

Zaoui, A., 1997. Structural morphology and constitutive behaviour of microheterogeneous materials. In: Continuum micromechanics. Springer, pp. 291–347.

Zhang, D., Liu, E. L., Huang, J., 2019a. Elastoplastic constitutive model for frozen sands based on framework of homogenization theory. Acta Geotechnica (2), 1–15.

Zhang, D., Liu, E. L., Liu, X. Y., Song, B. T., 2018a. Investigation on binary medium model taking frozen silt soils under -6°c for example. Chinese Journal of Geotechnical Engineering 40 (1), 82–90.

Zhang, D., Liu, E. L., Liu, X. Y., Song, B. T., 2018b. Investigation on strength criterion for frozen silt soils. Rock and Soil Mechanics 39 (9), 3237–3245.

Zhang, D., Liu, E. L., Liu, X. Y., Zhang, G., Song, B. T., 2017. A new strength criterion for frozen soils considering the influence of temperature and coarse-grained contents. Cold Regions Science & Technology 143 (nov.), 1–12.

Zhang, D., Liu, E. L., Liu, X. Y., Zhang, G., Yin, X., Song, B. T., 2018c. Investigation on the nonlinear strength properties and damage statistical constitutive model for frozen sandy soils. Advances in Materials Science and Engineering 2018, 1–15.

Zhang, K., Zhao, L. Y., Ni, T., Zhu, Q. Z., Shen, J., Fan, Y. H., 2019b. Experimental investigation and multiscale modeling of reactive powder cement pastes subject to triaxial compressive stresses. Construction and Building Materials 224, 242–254.

Zhang, T., Zhou, Y. W., Guo, D. X., Qiu, G. Q., Li, S. D., 2001. Geocryology in china. Arctic Antarctic & Alpine Research 33 (2), 245.

Zhao, L. Y., Shao, J. F., Zhu, Q. Z., 2018a. Analysis of localized cracking in quasi-brittle materials with a micro-mechanics based friction-damage approach. Journal of the Mechanics and Physics of Solids 119, 163–187.

Zhao, L. Y., Shao, J. F., Zhu, Q. Z., Liu, Z. B., Yurtdas, I., 2019. Homogenization of rock-like materials with plastic matrix based on an incremental variational principle. International Journal of Plasticity 123, 145–164.

Zhao, L. Y., Zhu, Q. Z., Shao, J. F., 2018b. A micro-mechanics based plastic damage model for quasi-brittle materials under a large range of compressive stress. International Journal of Plasticity 100, 156–176.

Zhao, Y., Han, Q. L., Zhao, Y. D., Liu, J. H., 2017. The research status and analysis of frozen soil interior materials

603 based on ct nondestructive scanning technology. Journal of Glaciology & Geocryology 39 (6), 1307–1314.
604 Zhao, Y. H., Lai, Y. M., Zhang, J., Bai, R. Q., 2020. A bounding surface model for frozen sulfate saline silty clay
605 considering rotation of principal stress axes. International Journal of Mechanical Sciences 177, 105570.
606 Zhou, M. M., Meschke, G., 2018. A multiscale homogenization model for strength predictions of fully and partially
607 frozen soils. Acta Geotechnica 13 (1), 175–193.
608 Zhu, Q. Z., 2016. Strength prediction of dry and saturated brittle rocks by unilateral damage-friction coupling analyses.
609 Computers and Geotechnics 73, 16–23.
610 Zhu, Q. Z., Shao, J. F., Kondo, D., 2011. A micromechanics-based thermodynamic formulation of isotropic damage
611 with unilateral and friction effects. European Journal of Mechanics-A/Solids 30 (3), 316–325.
612 Zhu, Q. Z., Shao, J. F., Mainguy, M., 2010a. A micromechanics-based elastoplastic damage model for granular
613 materials at low confining pressure. International Journal of Plasticity 26 (4), 586–602.
614 Zhu, Q. Z., Zhao, L. Y., Shao, J. F., 2016a. Analytical and numerical analysis of frictional damage in quasi brittle
615 materials. Journal of the Mechanics & Physics of Solids 92, 137–163.
616 Zhu, Z. W., Kang, G. Z., Ma, Y., Xie, Q. J., Zhang, D., Ning, J. G., 2016b. Temperature damage and constitutive
617 model of frozen soil under dynamic loading. Mechanics of Materials 102 (102), 108–116.
618 Zhu, Z. W., Ning, J. G., Ma, W., 2010b. A constitutive model of frozen soil with damage and numerical simulation
619 for the coupled problem. Science China Physics, Mechanics and Astronomy 53 (4), 699–711.